Detached eddy simulation of a closely running lorry platoon

Mingzhe He, Shen Ryan Huo, Hassan Hemida, Frederick Bourriez, Francis H. Robertson, David Soper, Mark Sterling, Chris Baker

Abstract

In recent years, the concept of autonomous road vehicles has gained a great deal of technical respectability, with expected fuel benefits arising from running vehicles closely in platoons. However, the aerodynamics of such vehicles travelling in close proximity is still not understood. This paper presents for the first time a detailed study of drag benefits and the flow structure around a platoon of high-sided lorries, through conducting Delayed Detached Eddy Simulations (DDES). The lorry surface pressure and slipstream flow characteristics show good agreement with experimental data. Drag reductions of up to 70% have been observed for all trailing lorries in the platoon. Analysis of the flow field indicated highly turbulent regions on the top and sides of trailing lorries. Turbulent kinetic energy and Reynolds stresses were found to concentrate at the connection region between lorry cab and box. Spectral analysis of the side forces identified oscillating behaviour on each lorry in the platoon due to strong vortex shedding, suggesting that platooning lorries are potentially more likely to develop lateral instabilities than an isolated lorry. The study indicates that autonomous vehicle developers and operators should consider the significant drag reduction benefits of platooning against the risk associated with potential lateral instabilities.

1. Introduction

Recent advances in technologies such as digital mapping, sensing and inter-vehicle communications have the potential to revolutionise road transport, enabling vehicles to safely travel in close proximity to one another at relatively high speed (Liaifar, 2013). This type of arrangement, which is commonly referred to as platooning, potentially has benefits through more efficient road usage and a reduction in transport costs through the reduction of drag force, and hence an increase in fuel efficiency. This concept is not new and is frequently illustrated in sports, e.g., motor racing, where it is commonly referred to as drafting or slipstreaming (Watts, 2015) and bicycle racing (Blocken et al., 2016). As reviewed by Schuetz (2016), both model-scale tests (Ewald, 1984) and field tests (Michaelian and Browand, 2001) showed the potential of driving in convoy in drag reduction and fuel saving. A photo of lorries in platoon on motorways can be seen in Figure 1.

Figure 1 Lorry platoons at The Brenner Pass ('Platooning', 2019)

Despite frequent examples of platooning in sport, there are a number of unresolved questions concerning the aerodynamics of close running vehicles, with only a limited amount of research undertaken in this area. Although experimental work has shown that significant drag reduction can be achieved for vehicles with different shapes when running in platoons at various inter-vehicle spacing (Zabat et al., 1995, Tsuei and Savaş, 2001), there has also been research (Pagliarella et al., 2007, Watkins and Vino, 2008), which have identified potential drag penalties for a two-vehicle platoon at small inter-vehicle spacings. More recent numerical campaigns include Large Eddy Simulations (LES) by Uystepruyst and Krajnović (2013), who observed drag reductions in keeping with Tsuei and Savaş (2001) for a four-cuboid platoon at relatively small inter-vehicle spacing. On two-vehicle platoons, considerable drag benefit was identified by Altinisik et al. (2015), based on the numerical and experimental study on a two-car platoon with various inter-vehicle spacings, for the lead car, especially with smaller inter-vehicle spacing, but no drag reduction was observed for the trailing car. LES of a similar type vehicle travelling in a two-vehicle platoon was also conducted by Mirzaei and Krajnović (2016) who again noted the drag penalty the when inter-vehicle spacing was equal to half of the vehicle length.

To date, a significant proportion of the existing research has focused on reducing the drag force in order to reduce fuel usage, especially for heavy-duty vehicles. RANS simulations have been undertaken by Vegendla et al. (2015), who focused on the drag reduction of vehicles running in tandem and in multi-lane scenarios. Humphreys and Bevly (2016) identified the drawbacks of Reynolds-Averaged Navier-Stokes (RANS) simulations compared to Detached Eddy Simulations (DES), based on the slipstream velocity prediction of a two-lorry platoon but confirmed the validity of RANS in predicting the overall trend of drag reduction for inter-vehicle spacings limited to four vehicle lengths. Recently DES methods have been used intensively for ground vehicles aerodynamics due to its low demand for computational resources and encouraging results have been shown to agree well with experimental data (Krajnović et al., 2007, Flynn et al., 2014, Ashton and Revell, 2015, Morden et al., 2015, Flynn et al., 2016, Humphreys and Bevly, 2016, Wang et al., 2017, Li et al., 2018). Bruneau et al. (2017) conducted Direct Numerical Simulations (DNS) on an isolated vehicle and platoons with two or three-vehicles, again with a focus on investigating potential drag reduction. Findings indicated significant drag reduction was achieved and it was noted that a three-vehicle platoon can achieve even better drag reduction compared to a two-vehicle platoon.

It is apparent that the existing research is limited to relatively short platoons, usually due to limited space in wind tunnels and the tremendous computational resources required for simulating long platoons. In addition, the vehicle shapes considered were commonly passenger cars or Ahmed bodies with various slant angles. Short platoons with a simple cuboid shape or simplified heavy-duty lorries were also considered but the corresponding simulations were mostly RANS. The focus was usually on reducing inter-vehicle spacing to achieve drag reduction, but any other effects are unclear. For example, the transient effects of the flow are commonly investigated through frequency analysis for a single vehicle (Grandemange et al., 2013, Lahaye et al., 2014, Volpe et al., 2015, McArthur et al., 2018) but largely overlooked for vehicle platoons. Moreover, the stability of vehicles running in platoon formation, which could be an important issue for safety, vehicle handling and the introduction of these technologies, is also rarely considered in the literature. Based on the clear need for greater understanding of the vehicle aerodynamic interactions and the possible effects of these, this paper presents work undertaken as part of an EPSRC funded project entitled 'The aerodynamics of close running ground vehicles - EP/N004213/1'. The aim of this project was to understand the nature of the flow between vehicles running in close proximity for a long platoon formation and identify the benefits of such operation and the aerodynamic problems that may result. A series of novel moving model scale experiments were undertaken at the University of Birmingham Transient Aerodynamic Investigation (TRAIN) rig facility to measure aerodynamic drag, identify loads on structural components and investigate lateral and vertical instabilities. Concurrently, computational fluid dynamics (CFD) simulations were also conducted using conventional RANS techniques for a wide range of vehicle and platoon configurations, but also a smaller number of cases using more sophisticated DDES methods to provide high-quality unsteady flow information. Taken together, the physical modelling results and the CFD simulations enable for the first time a detailed understanding to be achieved of the aerodynamic behaviour of ground vehicles running closely together. The work presented in this paper uses DDES to investigate the unsteady aerodynamic features of an eight-vehicle long platoon with relatively small inter-vehicle spacing. Full details of the experiments with different inter-vehicle spacings are not considered here, DDES results for the same platoon with crosswind and RANS results on the effects of varying inter-vehicle spacing and with different vehicle shapes and yaw wind conditions will be published in due course. A brief introduction to the experimental work, conducted for validation of the present DDES results, is given in section 2. The numerical details are specified in the next section. Section 4 shows the excellent agreement between the DDES results and the experiments. Full analyses of the flow around the platoon are presented in section 5 with discussions of the findings. The key conclusions are highlighted in section 6.

2. Description of the vehicle model and the experiments

The moving model aerodynamic experiments used to validate the present DDES results are firstly introduced in this section. The experiments were conducted at the TRAIN rig, which is a purpose-built facility designed to investigate the transient aerodynamics of moving vehicles through correctly simulating the relative movement of a vehicle with respect to a fixed ground plane (Baker et al., 2001). Model vehicles are propelled along a series of 150 m long tracks at speeds up to 75 m/s, dependent on model weight. An in-depth introduction of the general setup, modelling techniques and the firing mechanism of the TRAIN rig can be found in (Soper et al., 2017). A typical run of the test includes an acceleration stage immediately after firing. A pre-tensioned elastic bungee cord system is used to accelerate the platoon and no further propulsion

is used. The platoon then gradually reaches a constant maximum speed and travels along the track until reaching the deceleration section where the platoon is brought to rest through a friction braking device.

The vehicle shape used in this work is a 1/20th scale model of a box type lorry, simplified from a Leyland DAF 45-130, which has been studied extensively in (Quinn et al., 2007, Sterling et al., 2010, Cheli et al., 2011). The reason for studying this shape is because this high-sided lorry represents a 'typical' commercial vehicle (Quinn et al., 2007) and is similar to those which reportedly blow over during strong crosswind (Sterling et al., 2010). The relevant model-scale dimensions and overall shape of the model are given in Figure 2. The chosen number of eight lorries in the platoon was based on the knowledge of boundary layer development for bluff container freight trains, presented in (Soper et al., 2014). Golovanevskiy et al. (2012) also noticed that eight railcars are long enough to investigate the aerodynamic performance of the inner-cars within a long open cargo train. Pragmatically, this was also as long as could physically be achieved for the purpose of investigating long platoons. In order to overcome the difficulty of firing eight lorries simultaneously, a novel approach was applied in this study by which a set of model vehicles in a platoon configuration were mounted to a long spine type system. The whole lorry-spine system is propelled as a single unit so that the eight lorries move together with constant separation and run through a slot gap set between a suspended ground plane to simulate the normal ground condition. A photo of the physical platoon model on the elevated ground plane is shown in Figure 3. The suspended ground plane was positioned such that the platoon passes at a steady speed along a 4m test section. This 4m long section (equivalent to 10L), has 5 pairs of light gates positions at 1m intervals. The signals from these gates not only enable a check on the platoon speed to be undertaken but are also used to align the data from each model during data analysis. A light sensor on lorry 1, which also sends a signal to the remaining lorries, is used to sync the lorries with each other and the light gates.

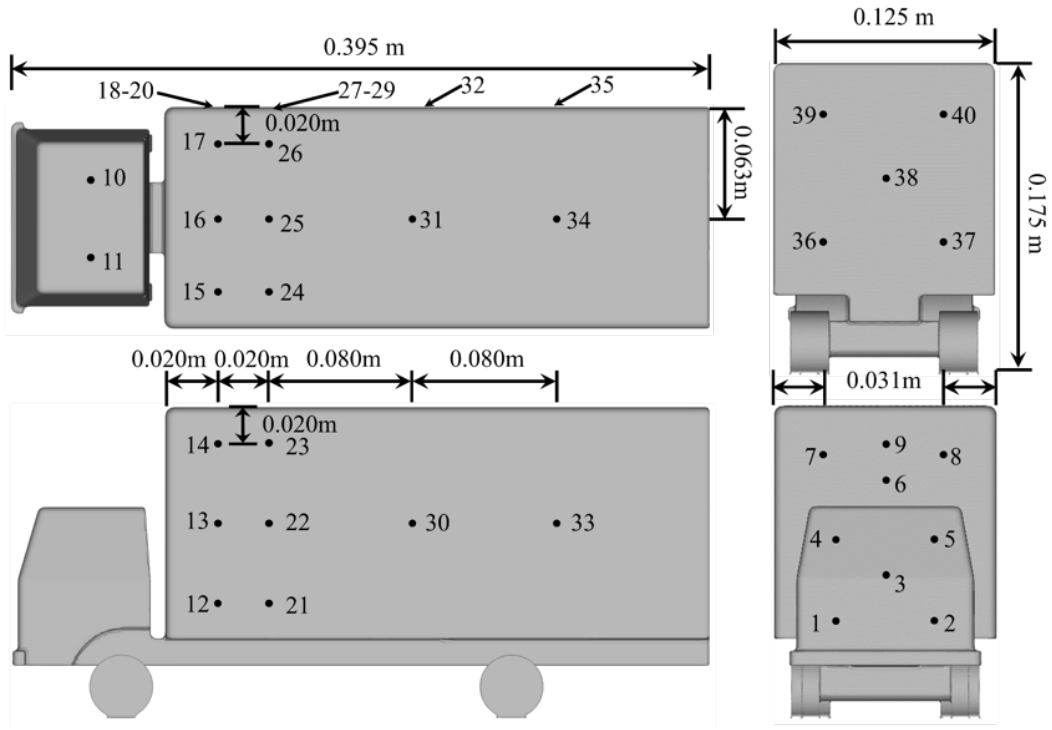

Figure 2 Key dimensions of the lorry model and the positions of the pressure taps

Figure 3 The lorry platoon model and the suspended ground plane used in the moving-model experiments

Surface pressure on the vehicle models was measured using FirstSensor Ltd pressure transducers and data was recorded using onboard data loggers. The data loggers are in-house built Arduino-based loggers recording 16 channels on MicroSD cards at a sample rate of 3000 Hz. Raw voltage data were then processed using MATLAB® to obtain pressure data by converting the voltage to pressure using transducer calibration profiles. As mentioned earlier, the ensemble averaging technique is employed due to highly variable time histories of velocity or pressure from individual measurement runs (Sterling et al., 2008). Under the current highly controlled experimental conditions, the behaviour of pressure or slipstream velocity in the 4-metre data taking section can be regarded as ergodic in which case the ensemble average is statistically the same as time average. As explained by Baker et al. (2001), a large number of runs (in the order of 10-20) are required to obtain the averaged results at discrete times or distances with regard to the nose of the first lorry in the platoon as such the standard deviation of the ensemble is comparable to the turbulence level. In the experiments, a series of 15 runs was found to provide statistically stable ensemble averages.

An illustration of the typical pressure data (Tap 3, lorry 1) recorded in 3 of the runs is shown in Figure 4. The pressure is non-dimensionalised by the measured vehicle speed through the test-section, while the x axis indicates the time before/after the first lorry passes the middle lightgate of the 4m section. It is apparent that the results from different runs are very consistent and the speed reduction when the platoon passes the 4m section is minimal. Thus, despite the very different nature of the moving-model experiments compared to conventional wind tunnel tests, the ensemble averaged results are comparable to the time-averaged data usually obtained from a wind tunnel or CFD.

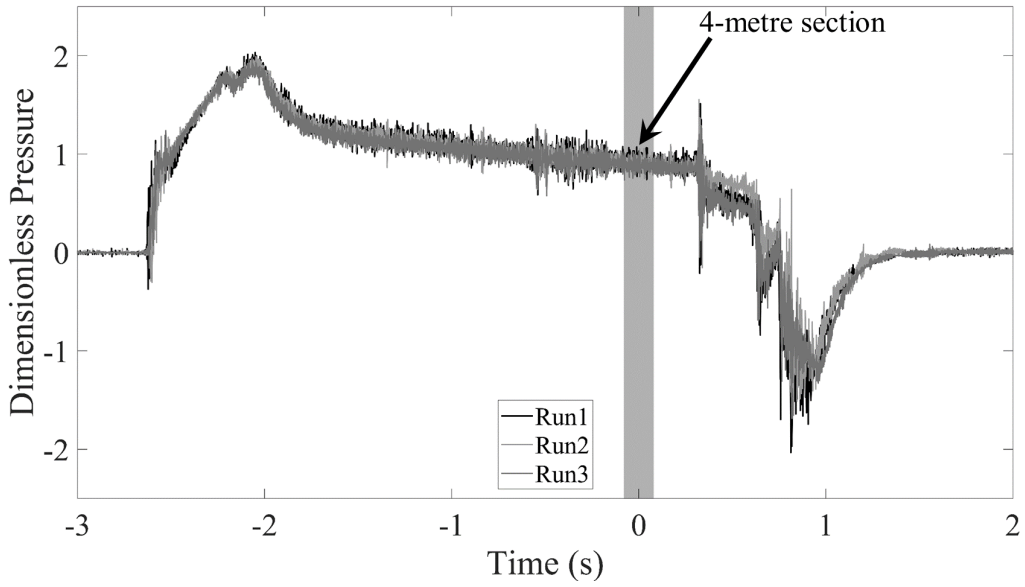

Figure 4 Representative plot of the dimensionless pressure data of Tap 3 on lorry 1obtained from 3 runs

Slipstream velocities were measured at the vehicle side and above the roof using multi-hole pressure probes (T.F.I., 2011). The three components of the wind were measured within a cone of influence of 45° and for a velocity vector higher than 2 m/s. All velocity data lower than 2 m/s were discarded. Velocity and flow direction uncertainties are within 0.5 m/s and 1° based on manufacturer specifications (TFI, 2011). Wind data were recorded at a sample rate of 5000 Hz and filtered to the probe maximum frequency response using a 650 Hz low-pass filter. Data were finally re-sampled to correct for differences in speed between runs. For ensemble averages of the slipstream measurements, a series of 20 runs were carried out for each measurement position. A schematic illustration of the slipstream measurement positions is given in Figure 5.

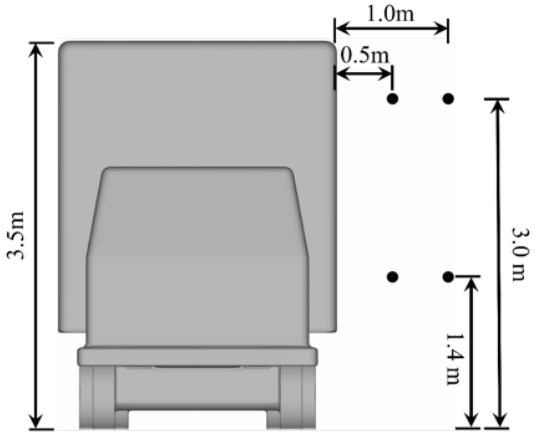

Figure 5 Schematic illustration of the slipstream measurement positions (dimensions in full-scale)

There were in total three different inter-vehicle spacings tested, namely 0.5L, 1.0L and 1.5L spacings, where L is the full length of the vehicle. The gaps were chosen after much reflection and build on existing work which can be found in the literature summarised in Section 1. As discussed, the 0.5L inter-vehicle spacing was chosen for this DDES study as experimental

(Robertson et al., 2018) and RANS (He et al., 2018a, He et al., 2018b) simulations highlighted that a platoon of lorries with 0.5L inter-vehicle spacing may potentially experience stronger flow-vehicle interaction. A detailed parametric study of the chosen range of inter-vehicle spacings will be covered by a subsequent paper and a separate experimental paper. There are of course potential measurement issues when the gap size reduces. At present, the smallest gap size was ~200mm at model scale (corresponding to 0.5L). To investigate smaller gaps risks generating conditions in the gaps which may not be representative of those at full-scale.

3. Numerical setups

3.1. Computational domain

The computational domain for a platoon of lorries employed in the present research is illustrated in Figure 6.

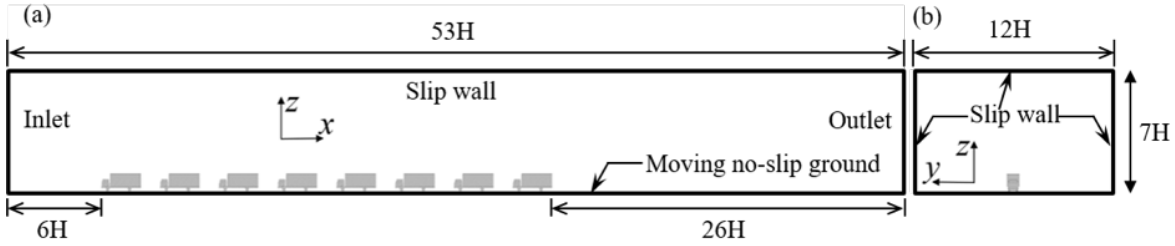

Figure 6 Computational domain. (a). Side view; (b). Front view

Figure 6(a) and (b) show the schematic side and front views of the entire computational domain, respectively. The inlet provides uniform flow at U_∞= 25 m/s, resulting in Reynolds number (Re) ≈ 3×10^5, based on the height of the lorry model. The inlet flow velocity is equal to that of the moving model vehicle speed in the experiments, which is 25 ± 1 m/s. Although all the vehicles are stationary with a no-slip wall boundary condition, the no-slip ground is moving at the same inlet flow velocity to simulate the relative motion between a running vehicle platoon and the stationary ground. The outlet is a zero pressure outlet, meaning that the reference pressure of the free stream p_∞= 0. The rest of the surfaces in Figure 6, namely the top and both sides, are all set to be slip patches.

Based on the definition of the coordinate axes in Figure 6, the aerodynamic forces, i.e. drag, side and lift forces are in the same direction of x, y and z axes, respectively and are defined as follows:

$$C_i = \frac{F_i}{\frac{1}{2}\rho U_\infty^2 A_f} \quad (i = D, S, L) \tag{1}$$

where F_D, F_S and F_L are effectively the drag, side and lift forces and thus C_D, C_S and C_L are the corresponding drag, side force and lift coefficients. A_f is the nominal area based, on which all the aerodynamic coefficients are calculated. It is the projected area of the lorry on the plane normal to the x axis.

3.2. Meshing

The computational meshes used in the current work were generated by the commercial software Hexpress/Hybrid (NUMECA International, 2017). The meshes are unstructured, dominated mainly by hexahedral cells. The cell number for the platoon is around 13 million and 52 million

for coarse and fine grids, respectively. An illustration of the computational meshes is presented in Figure 7.

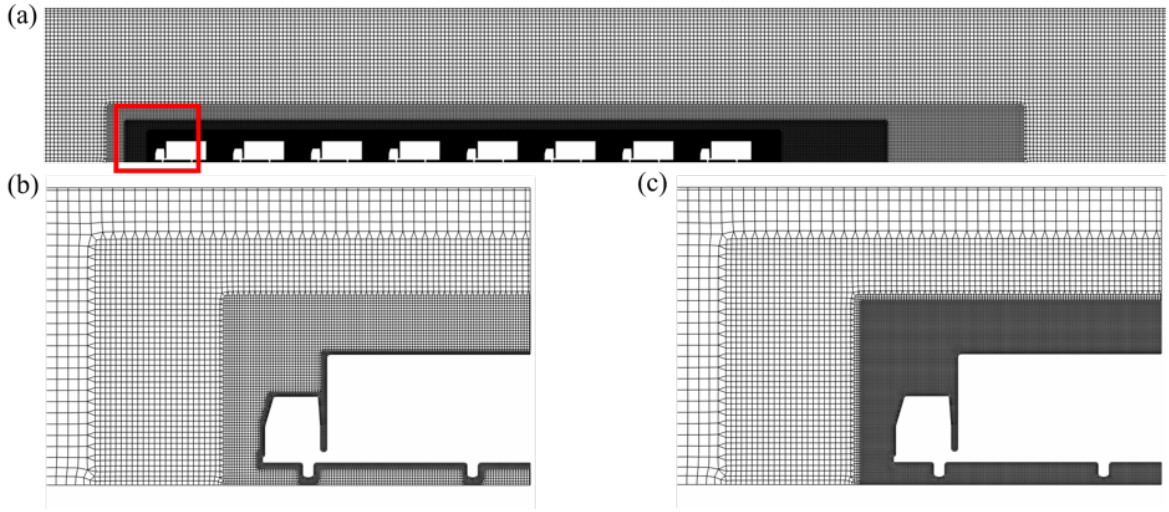

Figure 7 Computational mesh for the lorry platoon (a). full plane view; (b). coarse mesh of the selected region; (c). fine mesh of the selected region

As can be seen in Figure 7, multiple refinement boxes were introduced in order to make sure that the grid around the platoon is sufficiently fine and the use of the computational resources is concentrated on the most interesting regions where flow-vehicle interaction occurs. The averaged y+ values for the surface of the lorries in both meshes is around 70 and 30, respectively, with high values occurring only at a number of local cells.

3.3. Numerical schemes

The DDES approach, used in the present analyses, was introduced by Spalart et al. (2006), with the aim of providing an improved version of the conventional Detached Eddy Simulation (DES) through a hybrid approach that employs RANS with wall functions to solve the near wall flow and a LES approach for the detached flow. The hybrid methodology reduces the computational time required to resolve the near wall flow, especially for simulations with high Reynolds numbers (*Re*), but maintains good accuracy for bluff-body vehicle aerodynamics research (Hemida and Krajnović, 2009). The Spalart-Allmaras turbulence model was used as the closure model, which is suitable for the present mesh grids (Spalart and Allmaras, 1992). This one-equation turbulence model has historically been a popular tool due to its cost-effectiveness and robustness (Wasserman, 2016). Despite the potential drawbacks in predicting shear flow and under predicting separation, this method is believed to provide the most convenient length scale to inject grid spacing and turn a RANS model to SGS model (Travin et al., 2000). In addition, promising results had been obtained in research on similar problems (Kapadia et al., 2004, Maddox et al., 2004, Hemida and Krajnović, 2009, Flynn et al., 2014).

As to the numerical schemes, the convection terms were discretised using linear-upwind stabilised transport (LUST) scheme to achieve both stability and good accuracy. LUST discretisation scheme has a fixed blend of 75% second order central differencing scheme and 25% second order upwind scheme (OpenFOAM Ltd., 2016). Second order backward scheme was employed with a time step of $\Delta t=1\times10^{-5}$s, which lead to the mean and maximum Courant numbers throughout the domain around 0.01 and 2.3 respectively. The implicit PISO solver

was used with three correction steps and non-orthogonal correctors were used within each step. The time-averaging of velocity and pressure took place when the flow was fully developed along the whole platoon, which was ensured by monitoring the aerodynamic coefficients. A total of 10 seconds of averaging time was considered, which is equivalent to the flow passing the whole domain 30 times.

4. Validation of the DDES results

Results from the DDES simulation are compared with the aforementioned model-scale experiments in order to ensure the validity of the numerical simulation. Figure 8 and Figure 9 show a comparison between DDES and experimental data in terms of the lorry surface pressure coefficient (C_p) and normalised slipstream velocity in the along-wind direction (U_x/U_∞), respectively. It is worth reiterating that the experimental data used for validation are ensemble averages, which are compared with the corresponding time-averaged data from DDES.

The pressure coefficient, C_p, is a non-dimensional parameter defined as:

$$C_p = \frac{p - p_\infty}{\frac{1}{2}\rho_\infty U_\infty^2} \tag{2}$$

where p is the pressure, p_∞ is the reference pressure of the free stream, which is equivalent to the room atmospheric pressure in the experiment; ρ_∞ is the density of the freestream, equivalent to the room air density in the experiment and U_∞ is the inlet freestream velocity, which is the speed of the model platoon in the experiment. The uncertainty in C_p in the experiments is calculated as the sum of the bias limit (which accounts for the performance limits of the measuring equipment) and random uncertainty (which accounts for run-to-run variability due to flow unsteadiness) (Soper, 2016). The bias limit is calculated from propagation of uncertainty theory (Taylor, 1997) accounting for the individual biases in surface pressure, velocity and density. The random uncertainty is estimated at a confidence level of 95%, under the assumption that mean values from different runs are normally distributed (Taylor, 1997).

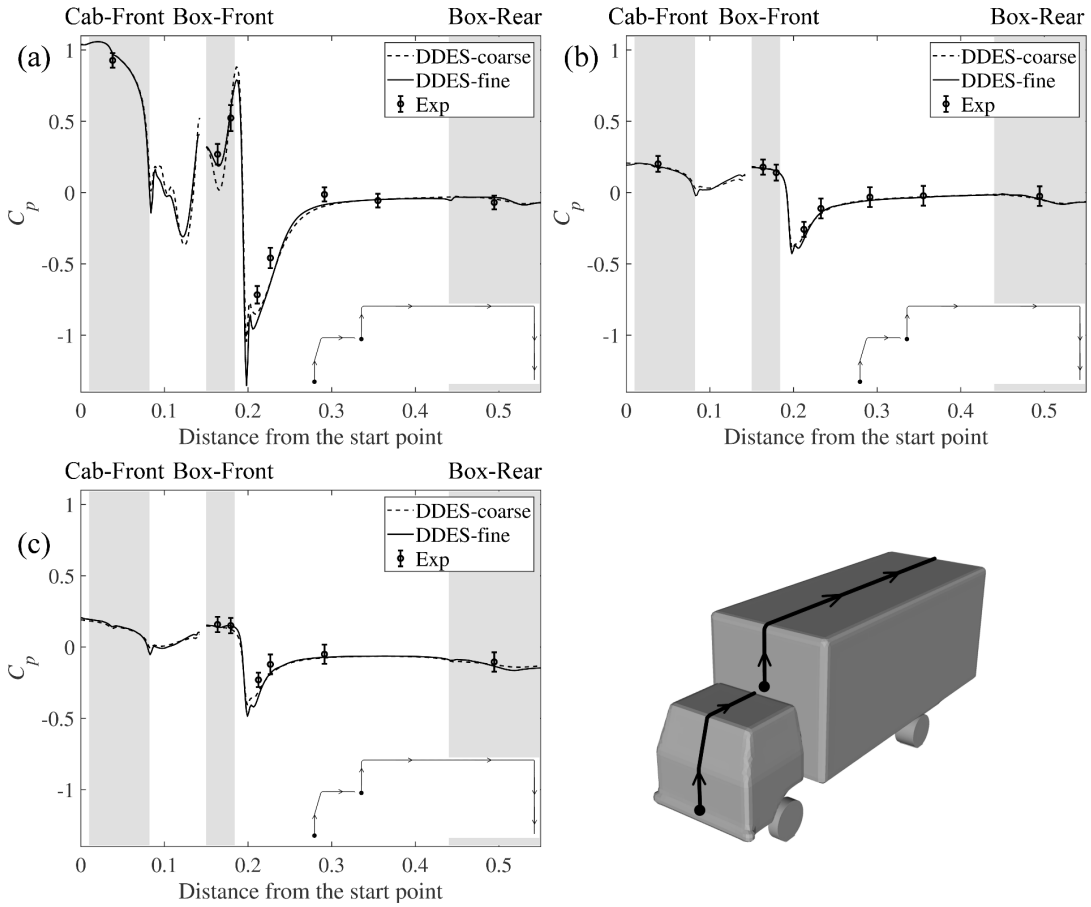

Figure 8 Surface pressure distribution along the middle of (a) lorry1; (b). lorry5 and (c). lorry8 validated against the moving model experimental data

Surface pressure results are shown in Figure 8 for lorries 1, 5 and 8 in the platoon, which represent the lead, the middle and the last lorry, respectively. The shaded areas are employed to distinguish in which regions of the lorry surface the pressure was taken. It is evident that the pressure distributions predicted by DDES with different grid densities are both generally in very good agreement with the experimental data for each lorry. Good agreement between coarse and fine grids suggests sufficient convergence to predict C_p. The results by the fine mesh grid generally provide slightly better agreement. Therefore, the analysis hereafter is based on the simulation with the fine grid.

The comparison of the slipstream velocity is shown in Figure 9, where U_x is normalised by the inlet velocity (U_∞ = 25 m/s). Two of the positions shown in Figure 5 are used as an example validation. The x axis is the normalised time $\tau=tU_\infty/l$, where t is time and l is the length of the lorry. With this convention, τ = 0 indicates the nose of the first lorry reaches the measurement probe while τ = 1 means that the rear of the first lorry left the measurement position.

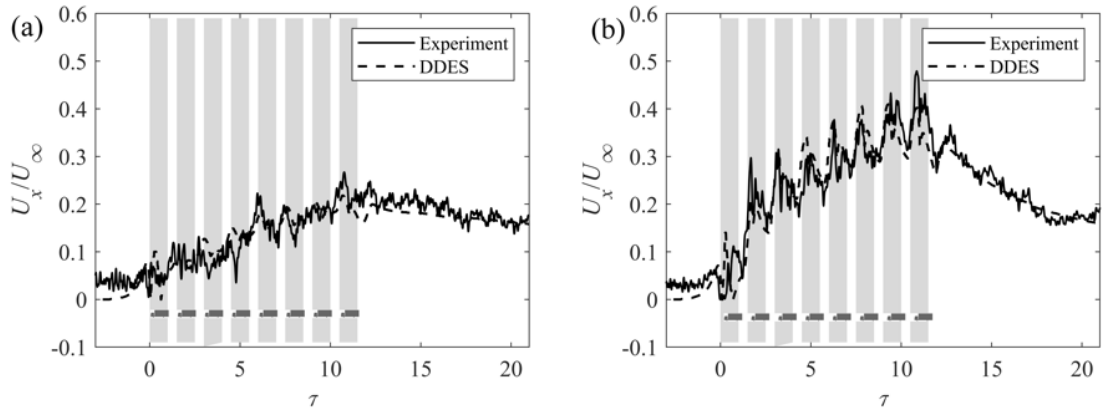

Figure 9 Normalised longitudinal component of the slipstream velocity against normalised time, Measurement position in full-scale at (a) 1.0 m from lorry side and 1.4 m above ground; (b) 0.5 m from lorry side and 3 m above ground

Again, Figure 9 demonstrates good agreement between the DDES simulation and experimental results for a range of measurement positions. For instance, there are clear peaks in velocity, as shown in Figure 9(b), corresponding to the front of each vehicle, which is accurately captured by the DDES. It is also worth mentioning that the patterns of the slipstream velocity and pressure coefficients of the current platoon show great similarity to those of a freight train with 50% and 33% loading efficiencies, especially the latter consist, as presented by Soper et al. (2014).

5. Results

5.1. The drag coefficient of each lorry in the platoon

Prior to the platoon simulation, a DDES simulation for a single lorry was also conducted as a reference point for the force coefficients measured on lorries in the platoon configuration. The lorry model has an overall nominal frontal area of 0.02 m^2, leading to a drag coefficient (C_D) of 0.67. Meanwhile, physical model experiments for a single lorry were also carried out, where the drag force (F_D) is estimated as the mean surface pressure integrated over a discretised geometry of areas normal to flow. The estimated drag coefficient of a single lorry is 0.63 ± 0.06. The uncertainty in C_D is estimated from the uncertainties in C_p for each tap by applying propagation of uncertainty theory (Taylor, 1997), under the assumption that values for each tap are independent. It should be noted that the estimated uncertainty in C_D may be less than the true error because it does not account for inaccuracies in the assumption of uniform pressure across each discretised area (Dorigatti, 2013). Good agreement is achieved between the present DDES and the model-scale experiment.

There are also two existing papers which provide drag coefficient information on a lorry with a similar shape, i.e., a LES investigation by Patel et al. (2013) and wind tunnel test by Cheli et al. (2011). Both works employed a single lorry model that kept most of the features of the original full-scale DAF lorry shape, including the door mirrors, under-body skirts etc. A comparison of the models used in the literature and the present work can be seen in Figure 10(a) and (b) respectively. It should be noted that the model used by Patel et al. (2013) was a $1/25^{th}$ model while the one investigated by Cheli et al. (2011) was in a $1/10^{th}$ scale. However, the *Re* numbers in both works are comparable to that used in the current work, i.e. in an order of 10^5.

Figure 10 is just to show the simplifications made for the model used in the current work compared to that in literature.

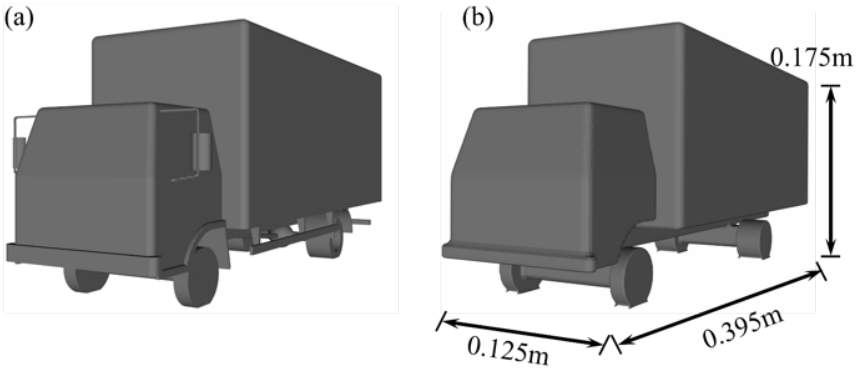

Figure 10 Model shapes (a) used in (Patel et al., 2013, Cheli et al., 2011); (b) used in present work

Although the current work uses a simplified shape excluding the aforementioned small features, these features are deemed to have negligible effects on the overall flow behaviour but only introduce small-scale turbulence (Baker et al., 2001, Dorigatti et al., 2015). Therefore, the drag coefficients of the two models presented in Figure 10 are comparable. Table 1 summarises the drag coefficients, calculated based on the same nominal frontal area, obtained the present DDES, the physical moving model experiments, LES (Patel et al., 2013) and the wind tunnel test (Cheli et al., 2011) respectively.

Table 1 Comparison of the drag coefficient between the present work and literature

	Drag Coefficient	Difference of the mean against DDES results %
Present work (DDES)	0.67	0.0
Moving model experiments	0.63 ± 0.06	6.0
LES (Patel et al., 2013)	0.61	9.0
Wind Tunnel (Cheli et al., 2011)	0.66 ± 0.09	1.5

As can be seen from Table 1, the drag coefficient obtained from the present DDES of a single lorry shows excellent agreement with the physical moving model experiments as well as those from the existing literature. It also confirms the negligible contribution of the small features to drag coefficients.

When the lorries are running in tandem formation, the drag coefficient of each lorry is compared with the estimation from the physical model results, as shown in Figure 11. The drag coefficients for an isolated lorry, as listed in Table 1, are also presented.

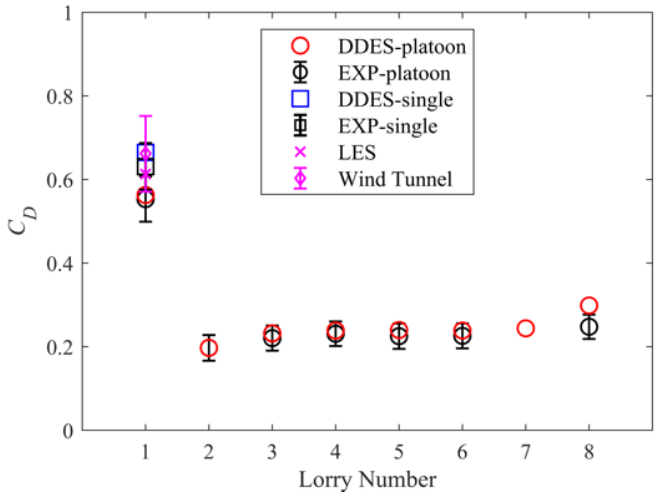

Figure 11 Drag coefficients of a single and a lorry in platoon predicted by the present work in comparison with single lorry drag from existing literature

As shown in Figure 11, the drag coefficients of the first lorry in a platoon and a single lorry predicted by the DDES simulations conducted in the present work are 0.57 and 0.67, respectively, which indicates a 15% drop in drag. This is due to the presence of lorry 2 which raises the rear pressure on lorry 1. A drastic reduction in drag (about 70%) due to the shielding effect of lorry 1 is observed for the second lorry followed by a gradual increase for the third lorry. There is then a gradual decrease in the drag reduction for the rest of the lorries until the last one where a noticeable increase in drag can be observed. The drag reduction of the intermediate vehicles, in general, is more than 60% while the last lorry has a drag reduction of about 55%.

The trend of drag reduction observed in the present DDES shows excellent agreement with the moving model test and is to some extent similar to the experimental (Tsuei and Savaş, 2001) and numerical (Uystepruyst and Krajnović, 2013) work on a four-cuboid platoon with 0.4L inter-vehicle spacing. Both works show that roughly 15% drop in drag can be achieved for the first vehicle, compared to an isolated cuboid. More than 60% and 70% drag reduction is achieved for the second and third cuboids, respectively, while about 60% reduction is achieved for the last cuboid in the platoon. It is interesting to notice that other work (Watts, 2015, Bruneau et al., 2017) on a 3-lorry platoon with squared-back tractor-trailers shape and similar inter-vehicle spacings also shows similar drag reduction trend, i.e. the first lorry reaches about 11%-15% drag reduction, although the second lorry has about 40%-50% drag reduction. The last lorry has slightly less drag reduction than the second one, achieving about 40%. The present analyses and literature all reported a slightly lower drag reduction for the last vehicle, largely due to the strong negative base pressure, which will be further discussed in section 5.2.

In comparison to other work on cyclists drafting (Blocken et al., 2018), it is interesting to find that the general trend of drag reduction is to some extent similar. Significant drag reduction can be experienced by the following cyclists, although the reduction is gradually increased as the cyclists are situated further into the cycling team until the 6th cyclist, which is different to the herein lorry platoon case. The drag reduction slightly decreases after the 6th cyclist and there is an obvious increase for the last one, which resembles the afore-discussed drag behaviour of the last lorry in the platoon. It is also worth mentioning that additive drag reducing

devices may also play an important role in reducing drag for vehicle platoons, which requires further investigation. However, the potential Reynolds number effects should be taken into consideration for model-scale investigation.

5.2. Overview of the flow field

The flow field of the lorry platoon is first examined through a series of contour plots to illustrate normalised mean velocity and dimensionless pressure coefficient (C_p). While C_p has been defined in Eq.(2), the velocity contour is based on the time-averaged velocity (U_{mean}) around the lorry platoon, normalised by the freestream velocity. The top view of a plane normal to the z axis and cut at $z/L \approx 0.25$ is presented in Figure 12.

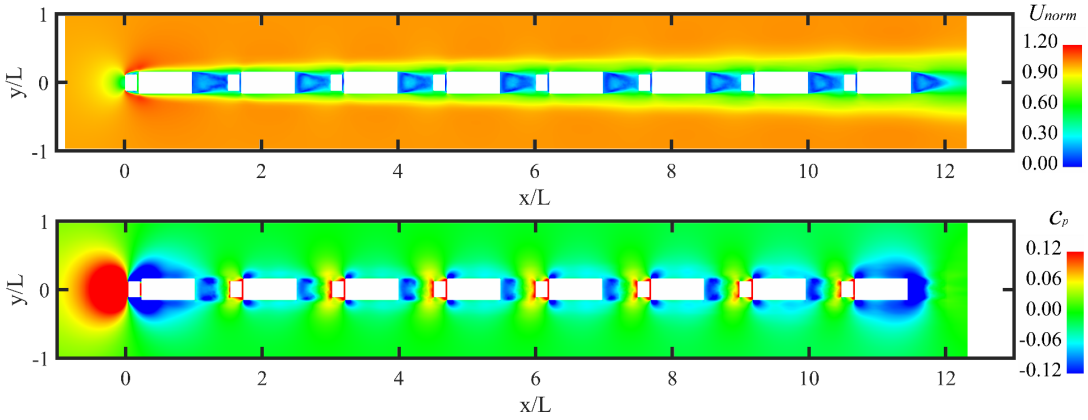

Figure 12 Top view of contours of time-averaged velocity (top) and pressure coefficient (bottom). z/L≈0.25

The normalised mean velocity (U_{norm}) contour in Figure 12 indicates that a thin symmetrical boundary layer is developed within which a low-speed region is observed at the gap between each lorry. Due to the low-speed region within the spaces between vehicles, there is a reduced frontal positive pressure for the trailing vehicles. This upstream pressure created by the trailing vehicles causes less negative surrounding pressure around the lead vehicle, especially the base pressure. As clearly indicated in the pressure contour, the last lorry in the platoon experiences a reduced positive pressure at the nose but greater negative pressure at the rear surface, due to the lack of following vehicle. Therefore, the first lorry experiences higher drag due to the high frontal positive pressure, compared to the trailing lorries, while lorry 8 may also be subject to relatively higher drag, compared to all other trailing lorries due to additional negative pressure at the rear surface.

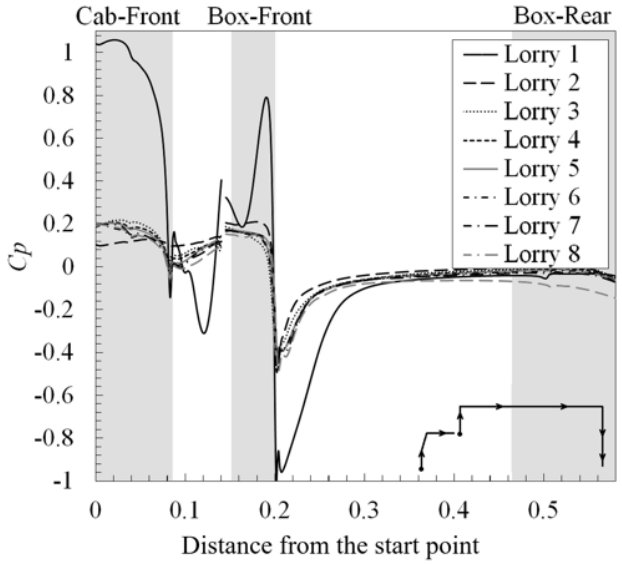

Figure 13 Surface pressure distribution along a cross-sectional line (y/L=0) cut in the middle of each lorry

Figure 13 illustrates a comparison of the pressure distribution along the central line from the front to the rear of each lorry in the platoon. The shaded areas represent at which part of the lorries the pressure is measured, denoted by the texts on the top of the figure. There is an evident reduction in magnitude of pressure for all trailing lorries compared to that for the first lorry. The first lorry in general experiences much higher positive pressure at the front of the cab and box. As a result of the shielding due to lorry 1, the front pressure for all the trailing lorries is much less than the first lorry. The most dramatic pressure changes at the top of the cab and the top frontal edge due to strong flow separation can also be found for lorry 1 compared to the rest of the lorries in the platoon, which is more evidently shown in Figure 14. Most of the top and the whole rear surfaces of the lorry box for lorry 1 to 7 exhibit a similar negative pressure distribution. However, there is an apparent drop in the negative pressure at the rear surface of lorry 8. In general, the pressure distribution shown in Figure 13 agrees with the pressure contour illustrated in Figure 12 and suggests the same trend of drag coefficient plot for the lorries in the platoon as seen in Figure 11. It is worth noting that the pressure distribution curve for lorry 2 follows a similar trend to that of other trailing lorries. However, a noticeable difference can be observed at the whole cab region as well as the box top surface where flow separates.

Figure 14 shows the side view of contours of the instantaneous vorticity, time-averaged turbulent kinetic energy and Reynold stresses in the streamwise and vertical direction of lorries in the platoon. Vorticity (ω) is mathematically defined as the curl of the velocity vector, which shows the local rotational motion of a particle in the fluid. Turbulent kinetic energy (TKE), denoted by k herein, is the kinetic energy per unit mass of the turbulent flow, measured by the velocity fluctuations. The Reynolds stresses signify the momentum transport due to turbulent fluctuations (Blazek, 2015). The Reynold stresses in the streamwise and vertical direction ($U'W'$) shown in the bottom of Figure 14 represents the flux in the vertical direction due to the fluctuating velocity in streamwise direction and vice versa.

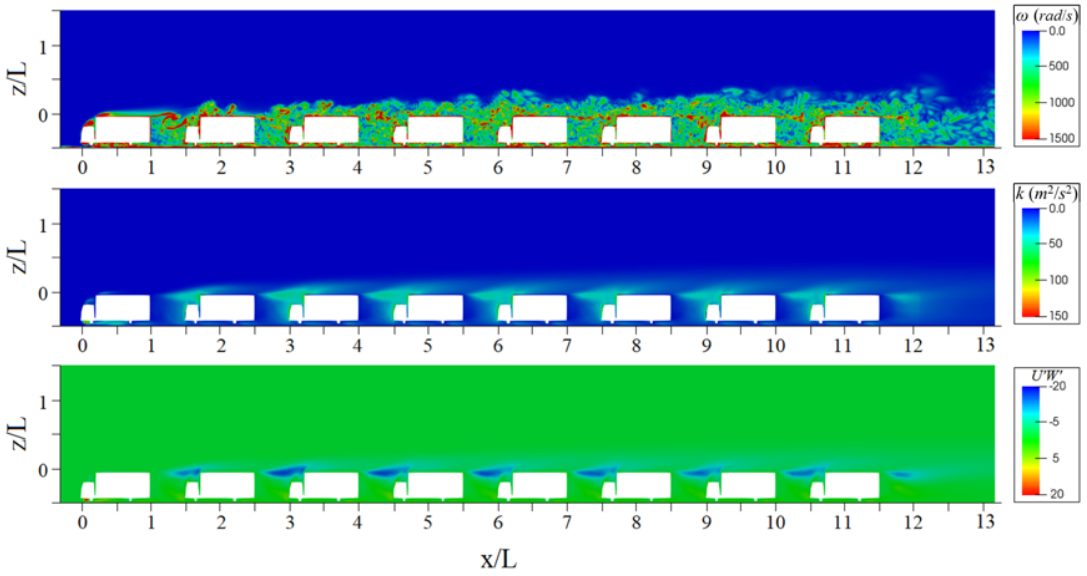

Figure 14: The contours of the instantaneous vorticity, time-averaged turbulent kinetic energy and Reynold stress in the streamwise and vertical direction of lorries in the platoon on the horizontal plane of y/L=0.

From the contours of vorticity, it can be observed that the flow around the first lorry has a unique pattern in comparison with the other lorries, which indicates strong separation of the flow at the top of cab and front edge of the lorry box. All the trailing lorries are immersed in the downstream turbulent flow generated by the first lorry. The concentration of turbulent kinetic energy can be seen at the top of the cab, as well as the front edge of the box, which means the flow in these regions is highly transient. Thin shear layers can be observed at the rear section of the box on all lorries and grow from the rear edge of the lorry towards the front of the following one. The Reynolds stress contours agree with the *k* contour, indicating strong stresses on top of the driver cab. The negative sign of the flux momentum term (*U'W'*) indicates the direction of the vertical flux due to streamwise momentum, suggesting transport into the inter-vehicle spacing.

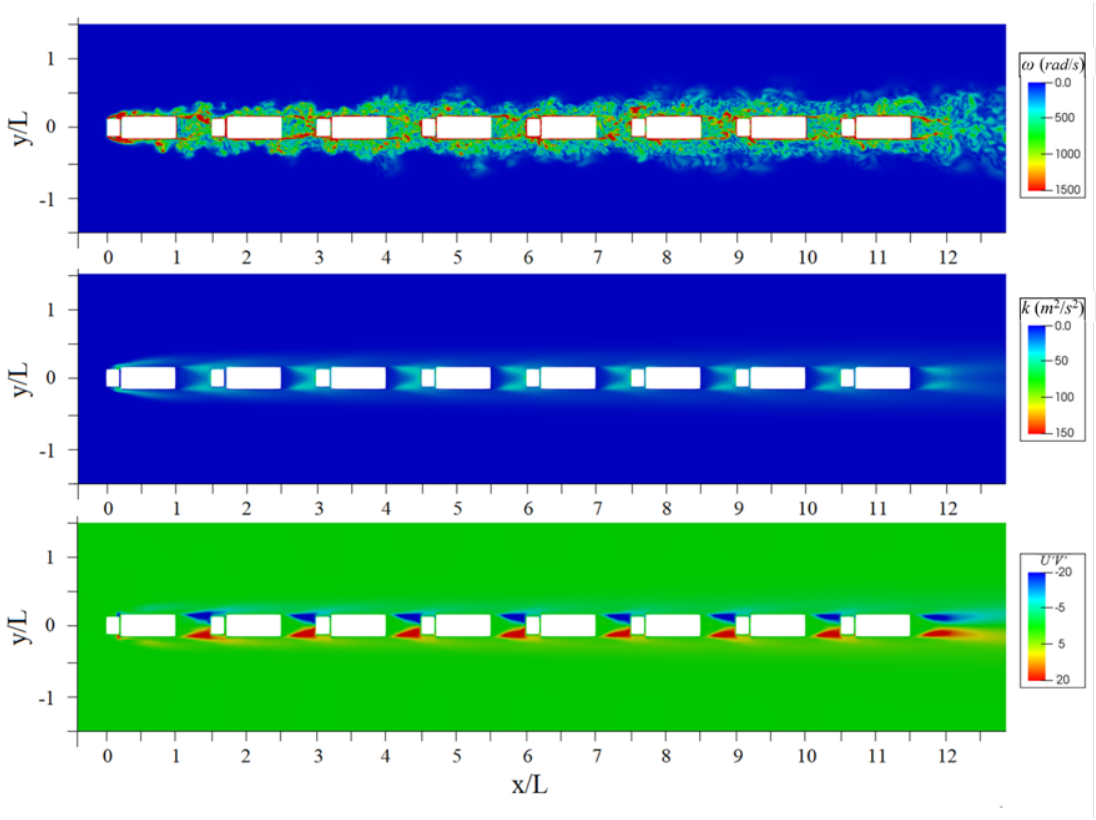

Figure 15: The contours of the instantaneous vorticity, time-averaged turbulent kinetic energy and Reynold stresses in the streamwise and span-wise direction of lorries in the platoon on the horizontal plane of z/L=0.25.

Figure 15 again shows the contours of the instantaneous vorticity, time-averaged turbulent kinetic energy and Reynold stresses in the streamwise and span-wise direction of lorries in the platoon but from the top view. Similar to the vorticity contour shown in Figure 14, it can be seen that the all lorries experience the downstream turbulent flow generated by the first lorry. However, the concentration of turbulent kinetic energy and Reynold stresses in the streamwise and span-wise direction are concentrated between the gaps of the lorries, especially in the nose region of the driver cab. Thin shear layers can again be observed spanning from both sides of the rear edge on all lorries. The sign of the Reynolds stresses again indicates the flux in spanwise direction due to streamwise momentum is towards the centre of the inter-vehicle gap.

5.3. Time-averaged flow field

In order to investigate the time-averaged flow field quantitatively, a number of measurement positions were taken, as illustrated in Figure 16.

Figure 16(a) shows that the vertical profile lines along the centre line (y=0) of the lorry are evaluated at different regions: the top of the cab, top of the box and the wake region of the lorry. The top of the cab consists of three vertical profiles, corresponding to x/L=0.05, 0.1 and 0.18; top of the box consists of four vertical profiles, corresponding to x/L=0.23, 0.3, 0.38 and 0.5; wake region of the lorry consists of four vertical profiles, corresponding to x/L=1.02, 1.14, 1.26 and 1.39. In addition, out-of-plane spanwise profile lines were taken at all aforementioned streamwise locations and at the height of z/L=0.24.

Figure 16(b) shows the horizontal profile lines with different heights, corresponding to z/L=0.45, 0.47 and 0.5, while the profile with the height of z/L=0.45 is situated on the top surface of the lorry. The horizontal lines extend from x/L=0 to 14.

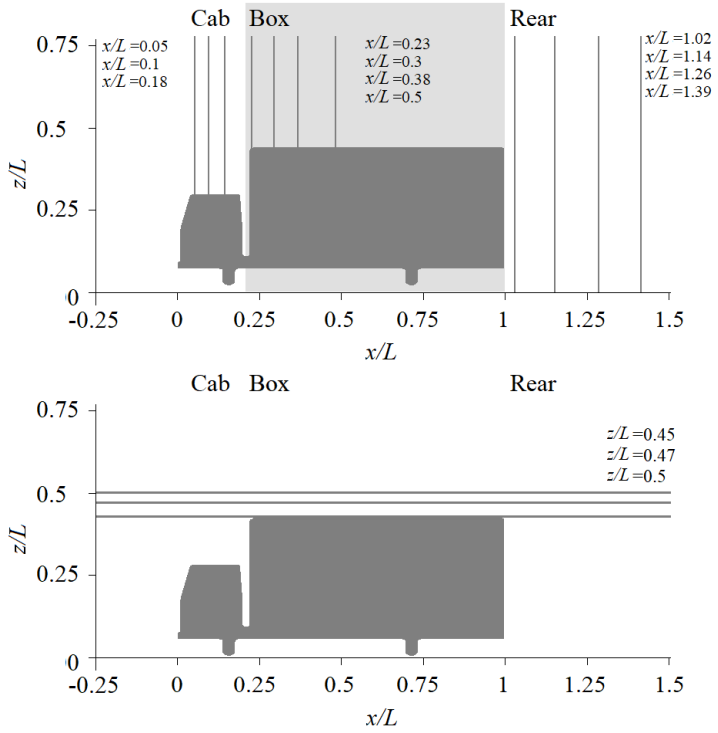

Figure 16: Location of the profile lines (a). vertical lines at different sections of the lorry; (b) horizontal lines at different heights above the lorry

Figure 17 shows the comparison of the vertical distribution of mean streamwise velocity profiles taken from profile lines shown in Figure 16(a). For the lines plotted in the same graph, they are separated by a uniform horizontal offset of 1.5 unit length. Development of the boundary layer along the platoon can be observed on the top surface of the lorry cab and box. After the initial disturbance over lorry 1, the boundary layer gradually forms as the flow goes down toward the rear of the platoon. As can be seen in Figure 17, the velocity distributions are significantly less distinguishable between lorries situated further back into the platoon. Therefore, it seems that the shape of profile curves for the trailing lorries is based on the position of the lorry in the platoon, i.e. the latter the lorry situated in the platoon, the less gradient observed on the profile curves. For example, the mean velocity profiles of lorry 2 are much less obvious than those of lorry 1 but still noticeably evident compared to all the rest of the trailing vehicles. This indicates a change of the flow structure for lorries situated further back into the platoon and the as the boundary layer develops. The region in the gap between two lorries has a very different flow pattern. Below the height of z/L=0.45, all lorries predicted very consistent velocity profiles, while regions above that height have greater magnitudes of the streamwise velocity apart from lorry 1, which agrees with the TKE and Reynolds stresses contours in Figure 14.

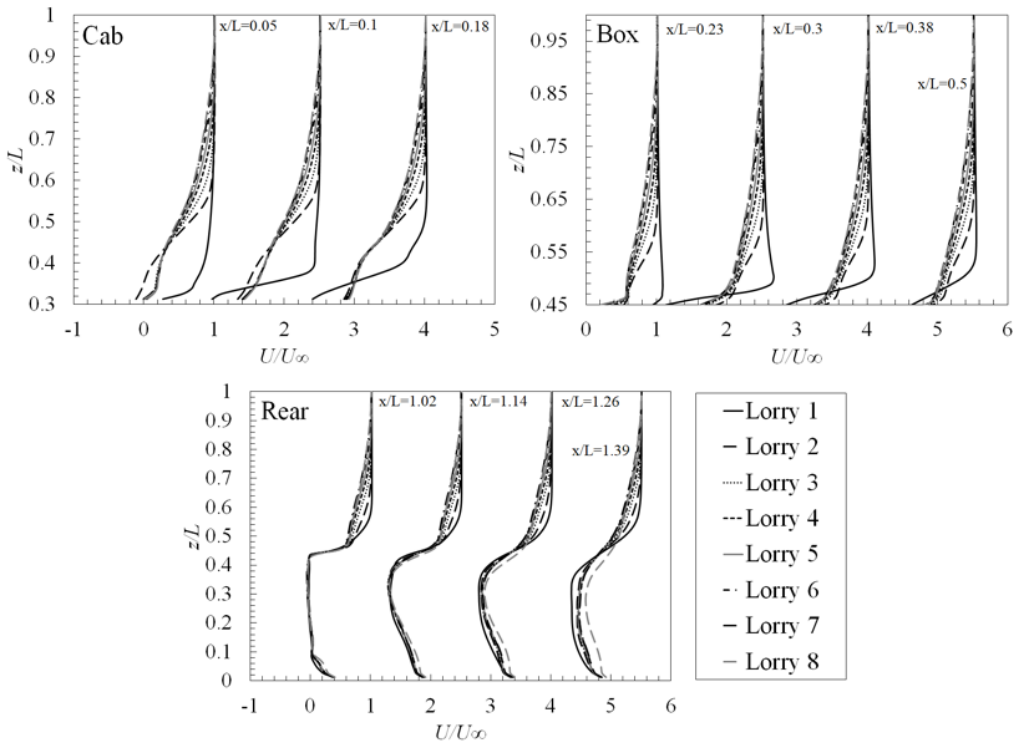

Figure 17: Vertical mean streamwise velocity profiles from different regions. Individual profiles are separated by a horizontal offset of 1.5, with the corresponding zero lines located at 0, 1.5…4.5.

The features shown by the curves in Figure 17 are further explored by detailed flow structure illustrations around the first, one of the middle (using the 5th lorry as an example) and last lorry, as can be seen in Figure 18. It should be noted that the overall flow structure for all the intermediate lorries is similar, especially when compared to the lorries at both ends, despite the slight difference caused by the development of the boundary layer. Thus, only lorry 5 is used as a representative of the intermediate lorries.

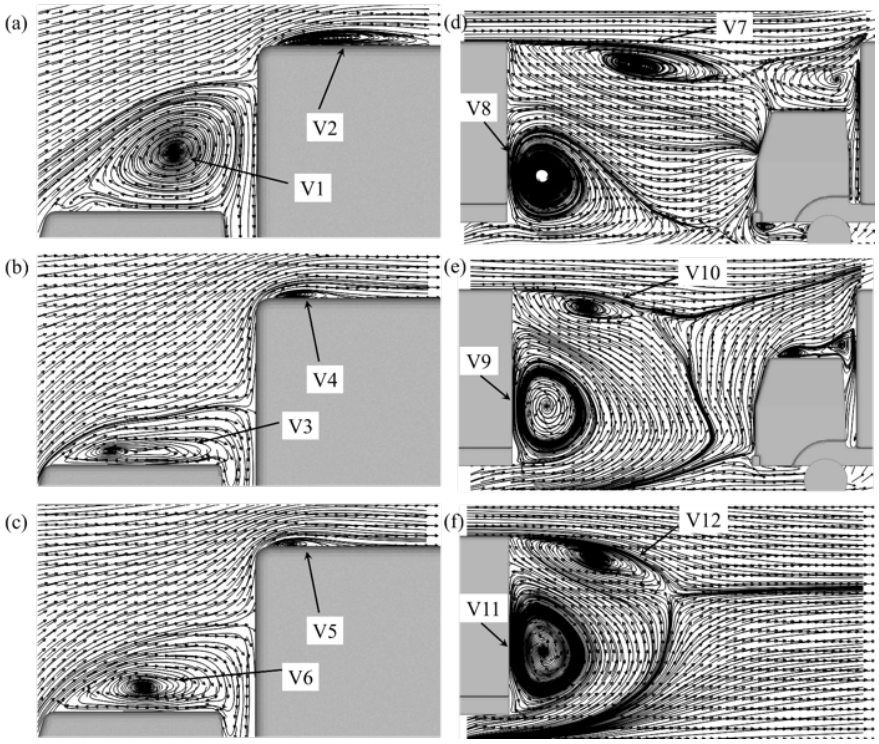

Figure 18 Detailed illustrations of the flow structure of three representative lorries in the platoon. Plane view at y/L=0 (a) lorry1-front; (b) lorry5-front;(c) lorry8-front;(d) lorry1-wake;(e)lorry5-wake;(f)lorry8-wake

As clearly indicated in Figure 18(a), (b) and (c), the recirculation (V1) on the top of lorry 1 cab is obviously much larger than that of lorry 5 (V3) and lorry 8 (V6). Thus, significant fluctuations of the velocity profiles above the cab of lorry 1 were observed in Figure 17. Similarly, in the region close to the front edge of the lorry box, much larger separation zone V2 was identified on the top surface of lorry 1 box, while recirculation zones for the two trailing lorries, i.e. V4 and V5 were formed with a much-reduced size. This explains the different behaviour between the lead and the trail lorries observed at x/L=0.3 on the top surface of lorry box, i.e. the profile line is still in the flow separation zone for the lead lorry but in the flow reattachment region for the trailing lorries. That also explains why the velocity profiles are similar for all the trailing lorries at $x/L \geq 0.3$, as is shown in Figure 17. The difference in the separation zones shown in Figure 18(a), (b) and (c) can also be used to elucidate the pressure difference between the lead and trailing lorries observed in Figure 13. For instance, the reason why the top surface of the lorry 1 cab experiences much larger pressure changes, as was seen in Figure 13, is apparently due to the much larger separation, V1, compared V3 and V6 for the two trailing lorries. The difference between V2, V4 and V5 is in keeping with the trend of pressure fluctuations on the top surface of lorry box in Figure 13. V2 signposts much stronger flow separation compared to V4 and V5, which leads to the more drastic drop of C_p at the front edge of the lorry 1 box. The longitudinal size of V2 is also greater V4 and V5. Thus, it leads to a delayed recovery of C_p from negative to almost zero in Figure 13 along the middle cross-sectional line of lorry 1 box.

Figure 18(d), (e) and (f), on the other hand, show the flow structures in the wake region of lorry 1, 5 and 8, respectively. There are apparently two major recirculation zones behind each lorry. The unique patterns of the recirculation pairs shown in the figure indicate the difference between the wake flow of the lead, middle and last lorries. To be more specific, the size and

longitudinal location of V7, V10 and V12 are dissimilar to each other. Another obvious difference lies in the longitudinal length of the envelope of the recirculation pairs. For instance, the wake recirculation region behind lorry 1 extends from the rear and ends up with hitting the front of the cab of lorry 2, resulting in the flow stagnation point at a relatively high position of lorry 2 nose, compared to that of lorry 5. The envelope shrinks in the longitudinal direction as the lorry is situated further into the platoon. As can be seen in Figure 18(e), with a slightly increased V9 but much-reduced V10, the envelope of the recirculation pair behind lorry 5 was shortened far before reaching to the nose of lorry 6. The envelope further decreased its longitudinal length in the wake of lorry 8, although the size of the top recirculation zone, V12 is larger than V10 while V11 remains similar to V9. The reason for that can be attributed to lack of following lorry to "push" the flow towards the upstream direction, leading to a large proportion of the flow directly running away to downstream. The decrease of the longitudinal length of the wake recirculation envelope seems to cause the difference of the velocity profiles between the first, middle and last lorries at x/L=1.39, as was observed in Figure 17. To be more specific, it is evident that the flow is moving upstream at x/L=1.39, as can be seen in Figure 18(d). Moreover, it is evident that this profile line is located well within the recirculation envelope in the wake of lorry 1. When checking the same profile line in the wake of lorry 5, it is noted that it goes through the envelope. Therefore, the streamwise velocity is more or less zero along the profile line, as shown in Figure 17 due to velocity is mainly in z direction, shown in Figure 18(e). However, at the same position in the wake of lorry 8, as shown in Figure 18(f), the profile line is already outside the recirculation region, which is reflected by the flow travelling downstream. The difference between the profile line in the wake of lorry 1, 5 and 8 causes the velocity profile in the wake of the first lorry shifted towards negative value compared to the intermediate lorries, while the velocity profile of the last lorry at that position in the wake shifted towards a more positive value. It is also the reason why lorry 8 exhibits more negative pressure at the rear, as has been seen in Figure 12 and Figure 13.

Figure 19 shows the top view of the mean streamwise velocity profiles from different regions. Individual profile lines in the same figure are separated by a horizontal offset of 1.0 unit length. Similarly, the initial formation of the boundary layer can be observed on the sides of the lorry 1, while less dispersion of velocity profile can be observed as the flow moves towards the rear of the platoon. As can be observed in Figure 19, only slight changes in the velocity profiles can be perceived as the vehicle positioned in a further downstream location of the platoon. As for the rear region, all lorries have similar velocity distribution and consistent flow structure, especially for the intermediate vehicles. However, similar to Figure 17, the velocity profiles of the first and last lorries differentiate from those of the intermediate vehicles at the location further away from the back of the lorries, e.g. x/L=1.39.

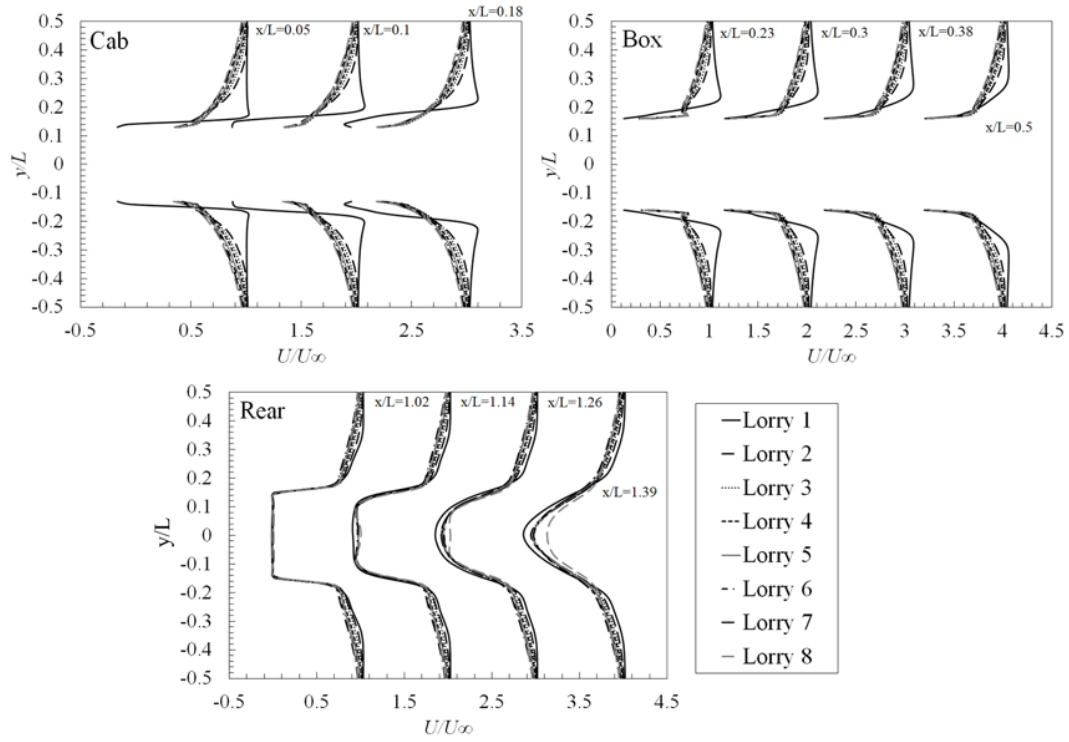

Figure 19: Horizontal mean streamwise velocity profiles from different regions at the height of z/L=0.24. Individual profiles are separated by a horizontal offset of 1, with the corresponding zero lines located at 0, 1…3.

Detailed illustrations of local flow structures from the top view are also provided, as can be seen in Figure 20.

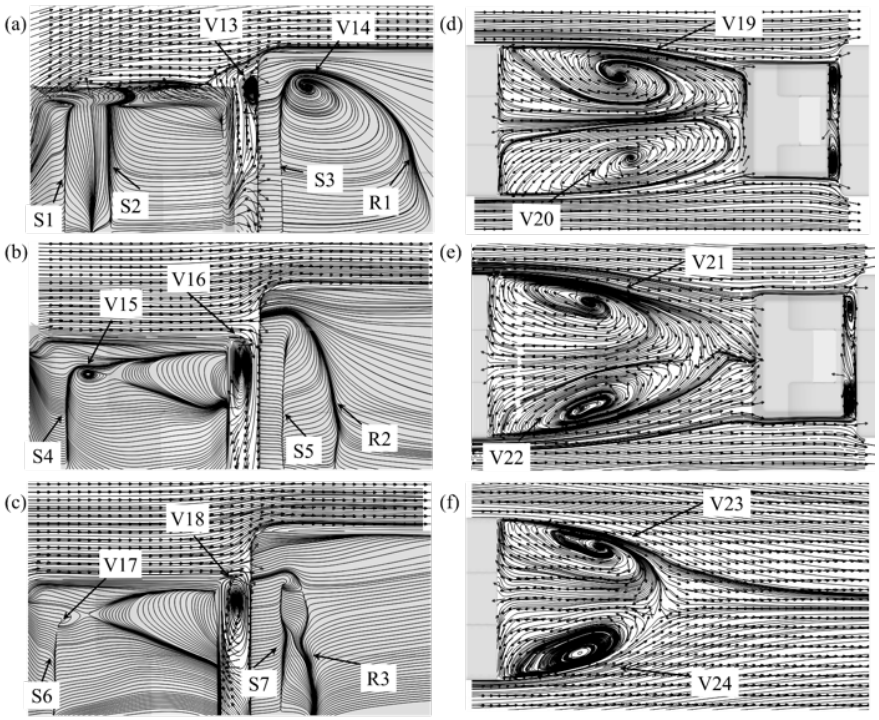

Figure 20 Detailed illustrations of the flow structure, as well as surface velocity traces of three representative lorries in the platoon. Plane view at z/L=0.24 (a) lorry1-front; (b) lorry5-front;(c) lorry8-front;(d) lorry1-wake;(e)lorry5-wake;(f)lorry8-wake

From Figure 20(a), (b) and (c), it is clear that strong separation occurs at the side of the driver cab of the lead lorry while negligible separation is identified for the trailing lorries, which leads to the large discrepancies of the velocity profiles between the lead and trailing lorries, as was observed in Figure 19. The flow pattern is much similar for the trailing lorries in the near wall region resulting in identical velocity profile in the near wall region for all the trailing lorries, as shown in Figure 19. Small recirculation zones were identified in the connection between the cab and box. Again, the trailing lorries show similar recirculation bubbles, i.e. V16 and V18, whereas the recirculation zone V13 for the first lorry exhibits a reduced size compared to V16 and V18. This difference results in the pressure discrepancy on the front of the lorry box in Figure 13. On the top of lorry box, flow separation and reattachment were observed. S3, S5 and S7 indicate where the flow separates, while R1, R2 and R3 denote where the reattachment occurs on the top surface of the lorry box of lorry 1, 5 and 8, respectively. These features together show that much stronger separation occurs on the lead lorry which takes a large region of the box top surface close to the front edge.

The top view of the wake region is illustrated in Figure 20(d), (e) and (f). Clearly, two counter-rotating recirculation zones dominate the wake of each lorry. As has also been identified in Figure 18, the longitudinal size of the recirculation region is the largest for the first lorry whereas the smallest for the last lorry. The intermediate lorries have more or less the same wake recirculation pattern with a medium longitudinal size compared to that of the lorries at both ends. This again corresponds to the discrepancies of velocity profiles at x/L=1.39 between the lorries at both ends and all the intermediate lorries.

In conclusion, based on the distribution of mean velocity flow field, several key features can be observed on all lorries. Two larger recirculation rings are observed at the rear, between the gaps of the lorries. While a thin recirculation ring is formed on the roof when the flow leaving the rear roof of the lorry, a much larger recirculation ring is formed close to the ground and covers most of the rear surfaces of the lorries. Evidently, high magnitudes of velocity fluctuation are located in regions contrary to where the recirculation rings occur, extending from rear edge of the lorry to the top cab region of the consecutive lorries. However, visible difference between the lorries at both ends and the intermediate ones can be noticed at locations further downstream in the wake, as indicated in Figure 17 to Figure 20. This causes a pressure difference on the lorries, which is the primary source of the increased drag force in relation to the other lorries in the platoon. The difference can also be identified through the flow stagnation point on the following lorry. For instance, the stagnation point of the front surface of lorry 2 is slightly higher than that of any other following lorries. This slight difference in flow structure around lorry 2 is probably the reason why the different pressure distribution, seen in Figure 13, is observed in comparison to the other trailing lorries. Minor recirculation zones can be observed on the top of lorries, among which the first lorry exhibits the largest recirculation. Small areas of high-velocity magnitude and fluctuations can be observed on the sides of the cab on lorry 1, but are absent for all other lorries.

5.4. Turbulence fluctuation

In this section, the root-mean-square (r.m.s.) velocity is used to evaluate the velocity fluctuation of the turbulent flow around the platoon.

Figure 21 shows the side view of the r.m.s. velocity fluctuations in the streamwise direction from different regions. Individual profile lines are separated by a horizontal offset of 0.5 unit length in the figure. High magnitudes of turbulent fluctuation are present at the region from the top surface of the cab to approximately the height of z/L=0.6 on all trailing lorries. The top of the trailing lorry box shows similar behaviour to the height of approximately z/L=0.85. It is worth mentioning that the velocity fluctuation is at a similar magnitude for all trailing lorries over a certain height above the top surfaces. For instance, the fluctuations are more or less the same for all trailing lorries from the top surfaces of the cab to about z/L=0.45. The fluctuation quickly falls to zero as the position on the profile line goes further above the top surface. However, there is an obvious trend that further back the position of the lorry sits in the platoon, the further above the top will the flow fluctuation exist. This also indicates the development of the overall boundary layer around the platoon. The rear of the lorries shows little to no turbulent fluctuation at the region where the recirculation occurs. However, high magnitudes of turbulent fluctuation occur above that region for all trailing lorries. The first lorry only shows limited flow fluctuations in terms of both magnitude and distance above the top surfaces, especially for the profile lines close to the front of the cab (x/L=0.05) and box(x/L=0.23), probably due to flow separation.

Figure 22 and Figure 23 show the top view of the vertical r.m.s. velocity fluctuations of different vehicle regions in the streamwise and span-wise direction, respectively. Individual profiles are separated by a horizontal offset of 0.3 unit length. Similar patterns with considerable magnitudes of velocity fluctuation in both the streamwise and span-wise direction can be observed on both sides of all the lorries in the platoon, excluding lorry 1. These high fluctuation regions extend from the side surfaces of the lorries to the distance of approximately y/L=0.25. At the rear region, the location of x/L=1.02 shows negligible velocity fluctuation at the recirculation zone, but a considerable magnitude at the sides from roughly y/L=0.15 to y/L=0.38 for all lorries. However, from the locations x/L=1.14 onward, two peaks of high-velocity fluctuation can be observed. These high levels of velocity fluctuation continuously increase and will extend to the top region of the consecutive lorry, as seen in the time-averaged flow shown in Figure 15. It is thought that these fluctuations are due to vortex shedding from both sides of the vehicle and the interaction of these flows with trailing lorries could potentially induce stability issues, as discussed below in section 5.5 through frequency analysis.

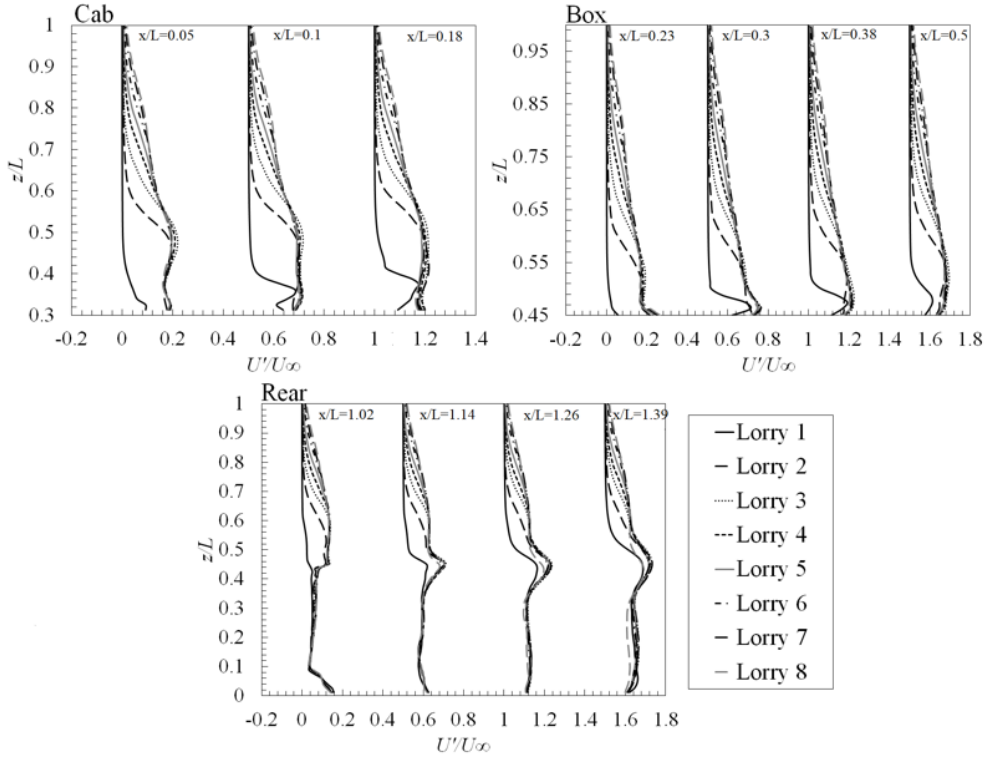

Figure 21: Vertical r.m.s. velocity fluctuations in the streamwise direction from different regions. Individual profiles are separated by a horizontal offset of 0.5, with the corresponding zero lines located at 0, 0.5…1.5.

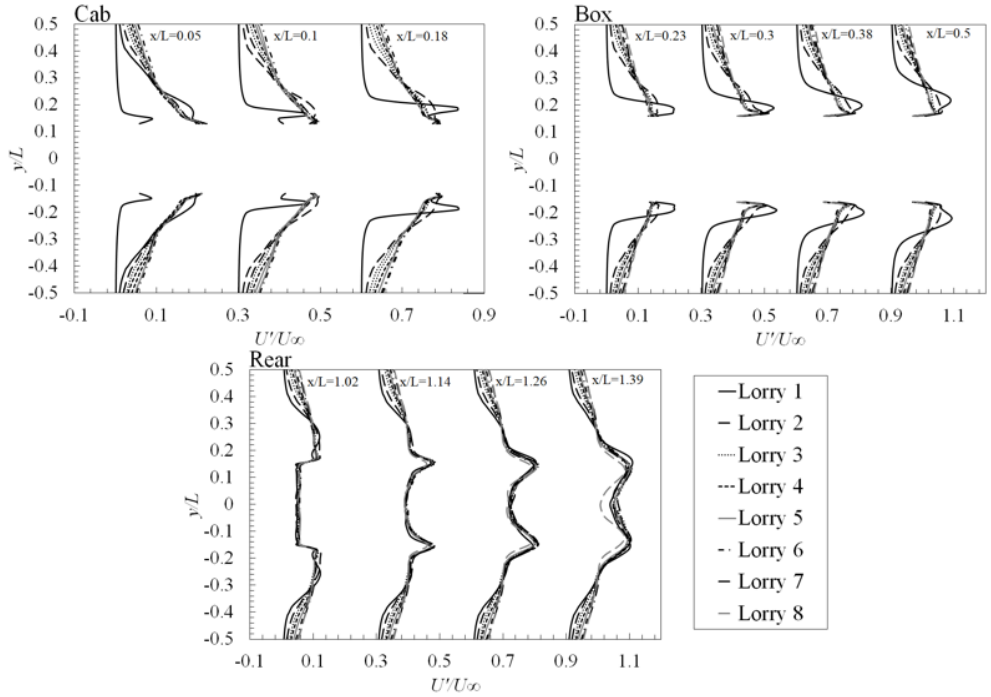

Figure 22: Horizontal r.m.s. velocity fluctuations in the streamwise direction from different regions at the height of z/L=0.24. Individual profiles are separated by a horizontal offset of 0.3, with the corresponding zero lines located at 0, 0.3…0.9.

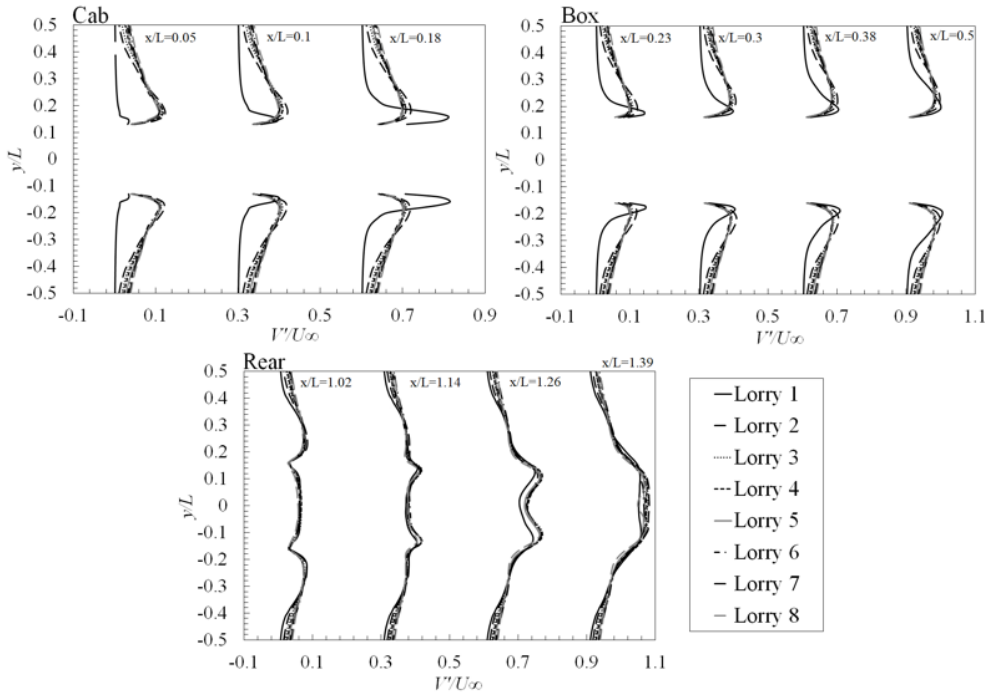

Figure 23: Horizontal r.m.s. velocity fluctuations in the span-wise direction from different regions at the height of z/L=0.24. Individual profiles are separated by a horizontal offset of 0.3, with the corresponding zero lines located at 0, 0.3…0.9

Figure 24 shows the horizontal distribution of TKE along profile lines at different heights at *z/L*=0.45, 0.47 and 0.5 above the lorries. The turbulent kinetic energy appears to be weakest on lorry 1, with a noticeable peak at the connection between the cab and the box at the height of *z/L*=0.47. The trend of TKE distribution is similar for all trailing lorries, where the highest spike locates at the connection between cab and lorry and the lowest values of TKE are situated at the rear end of the box closest to the surface at *z/L*=0.45. The highest spike value of TKE occurs at the front box edge of lorry 2. It gradually decreases as the lorry is situated further into the platoon. However, this decrease trend ceases from lorry 5 and the spike values of TKE for the latter four lorries remain more or less the same, despite some fluctuations. The reason for this trend of TKE spike values can be attributed to the velocity fluctuation shown by the profiles line *x/L*=0.23 in Figure 21-Figure 23. To be more specific, the profile line at *x/L*=0.23 for lorry 1 stays more or less constantly at 0 in Figure 21, which explains why the TKE of lorry 1 at this location is very small. Among all the trailing lorries, lorry 2 shows slightly higher velocity fluctuation at *x/L*=0.23 in Figure 21, which leads to higher TKE. In addition, more significant velocity fluctuations for lorry 2 at *x/L*=0.23, compared to other trailing lorries, can be observed in other planes, as shown in Figure 22 and Figure 23. Therefore, the overall velocity fluctuation, which is equivalent to TKE, is the highest at the front box edge of lorry 2. Following a similar approach, the aforementioned trend of the TKE spike values can be explained by the difference in velocity fluctuations of each lorry in the platoon. A considerable amount of energy is concentrated at the rear of lorry 8 but dissipates along the streamwise direction. This is also captured by the vorticity contour shown in Figure 14 and Figure 15, where strong vortices were generated from the top edge and two sides of lorry 8 box in the near wake, extending up to about x/L=12 but quickly dissipated beyond that region.

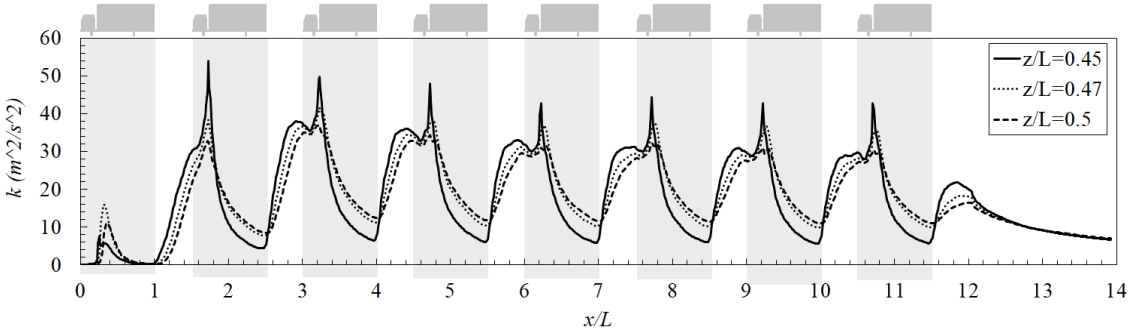

Figure 24: Horizontal distribution of turbulent kinetic energy at different heights above the lorries.

Figure 25 shows the horizontal distribution of Reynolds stress with the *U'V'* (streamwise span-wise direction), VW (span-wise vertical direction) and UW (Streamwise vertical direction) at different heights at z/L=0.45, 0.47 and 0.5 above the lorries. In general, the *U'V'* and *V'W'* components of Reynolds stresses are less significant in comparison, while the *U'W'* component circulates around the top cab region. Similar to the distribution of turbulent kinetic energy, Reynolds stresses are less significant over the length of lorry 1, whereas dramatic changes in magnitude are found within the gaps between lorries. The effects of Reynold stresses in the streamwise vertical direction is lowest on the lorry surfaces, but gradually increases as the height above the platoon increases.

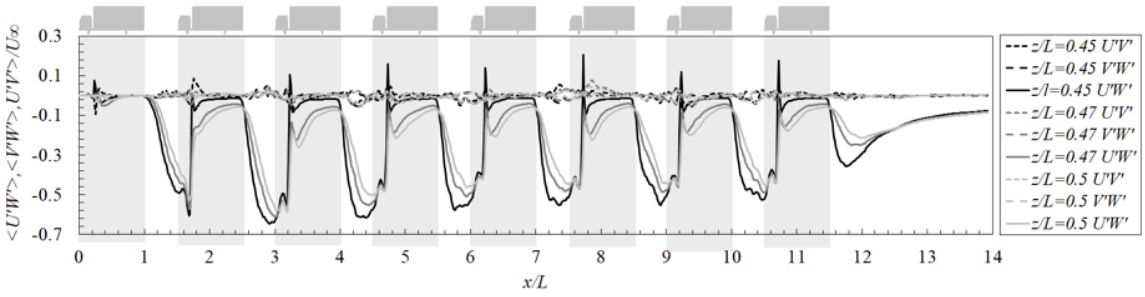

Figure 25: Horizontal distribution of Reynolds stresses at different heights above the lorries.

5.5. Frequency analysis of the forces on the platoon

Transient effects of the flow around the platoon, with special reference to the potential instability, are investigated through frequency analyses of the side forces on each lorry in the platoon. The time history data of the side force coefficient (C_S) of each model-scale lorry in the platoon is converted to the power spectral density (PSD) to search for any oscillating components of the side force that may cause lateral instability.

Figure 26 shows the PSD of an isolated lorry, normalised by its variance, which is plotted against the Strouhal number (*St*). *St* is equivalently a dimensionless frequency, defined as

$$St = \frac{fW}{U_\infty} \tag{3}$$

where *f* is the frequency of the flow, *W* is the characteristic length, which is the width of the lorry and U_∞ is the freestream velocity.

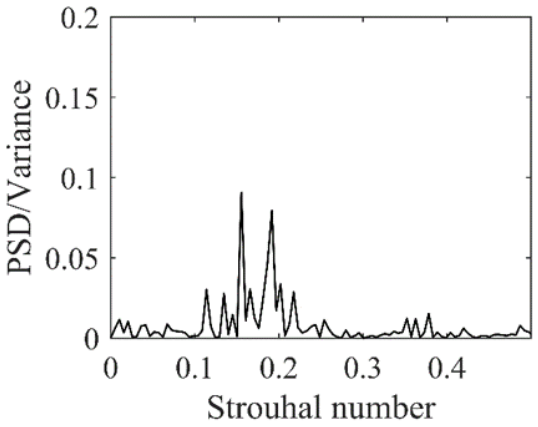

Figure 26 Normalised PSD of the side force coefficients against the Strouhal number for an isolated lorry

As clearly indicated in Figure 26, there are two distinct peaks of the oscillating components. The dominant component of the side force on a single lorry at $St \approx 0.16$ is close to the *St* found by Grandemange et al. (2013) ($St \approx 0.17$), Lahaye et al. (2014) ($St \approx 0.16$) and Volpe et al. (2015) ($St \approx 0.175$) for square back Ahmed body, which were related to vortex shedding generated from both vertical sides of the vehicle. The second major peak at $St \approx 0.19$ is very close to 0.2, which was reported by McArthur et al. (2018) for a heavy-duty tractor-trailer lorry with a square back.

Figure 27 shows the PSD of each lorry in the platoon. Again, the PSD is normalised by the variance and depicted against *St* based on the lorry width.

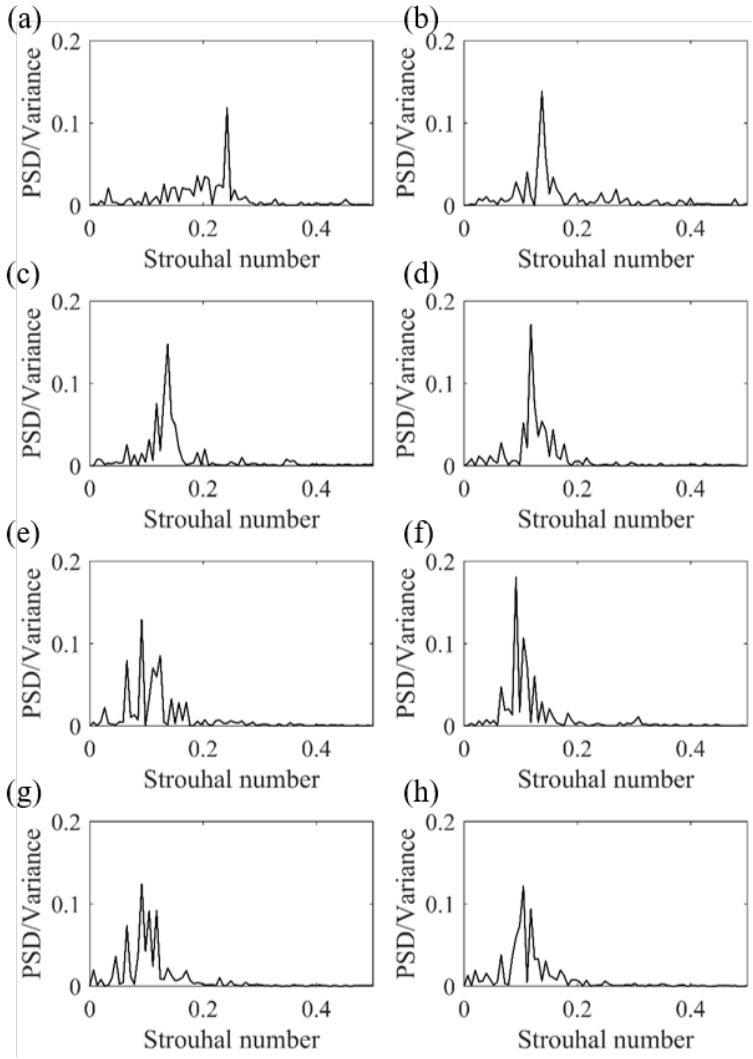

Figure 27 Normalised PSD of the side force coefficients against the Strouhal number for lorry 1 - 8

As can be seen in Figure 27, a number of peaks can be observed for each lorry in the *St* range of 0 to 0.5. A dominant frequency of the side force exists for each lorry in the platoon at relatively low frequencies. It is noted that only one distinct dominant component exists for the first four lorries in the platoon, while the dominant component is accompanied by a number of components with high power at various frequencies for the last four lorries. This implies that a single type of vortex shedding is dominating the lateral forces on the first four lorries but multiple modes may affect the latter four simultaneously due to highly turbulent flow. It is also worth noting that the power of the oscillating components after normalised by its variance, is less than 0.1 for an isolated lorry, as shown in Figure 26. However, the power of the dominant component of each lorry in the platoon is generally much higher than 0.1. This indicates that more powerful oscillating components from the side forces may act on lorries in a platoon. Therefore, there is more risk for a lorry in a platoon than an isolated one to develop lateral instability.

A summary of the variances of C_S, standard deviation (std) of the equivalent full-scale oscillating component, the dominate Strouhal number and the equivalent full-scale frequency of the oscillating components of an isolated lorry, as well as each lorry in the platoon, can be

obtained from Table 2. The equivalent std and frequencies are evaluated based on the maximum allowed lorry speed on dual carriageways in England, i.e. at 60 mph (~26.8m/s).

Table 2 The variance of the model-scale side forces and dominate Strouhal numbers

Lorry number	Variance of C_S ($\times 10^{-4}$)	std of the equivalent side force in full-scale (N)	Strouhal number (St) of the largest peak	Equivalent full-scale frequency (Hz) of the largest peak
Isolated	9.24	107.16	0.16	1.72
1	7.54	96.80	0.24	2.57
2	13.34	128.76	0.14	1.50
3	19.28	153.85	0.14	1.50
4	21.85	164.78	0.12	1.29
5	21.09	161.89	0.09	0.97
6	25.39	177.63	0.09	0.97
7	35.97	211.43	0.09	0.97
8	25.47	177.91	0.10	1.07

As summarised in Table 2, significant difference exists between each lorry in the platoon and an isolated lorry, in terms of both variance and St of the side force component. Due to the proximity of the trailing lorry, the dominant component of the side force on the first lorry in the platoon is now oscillating at a much higher $St \approx 0.24$ compared to that of an isolated lorry. However, the corresponding variance is less than an isolated lorry, which indicates less fluctuation of the instantaneous side force on the first lorry in the platoon than that on an isolated lorry. For all the trailing lorries, the dominant side force component is generally at lower oscillating frequencies but higher variances, compared to that of an isolate lorry.

Within the platoon, a general impression can be made that the further into the platoon of a lorry, the lower St but the higher variance of the dominant lateral force component can be found, except for the last lorry. There seems to be a correlation between the oscillating side forces on each lorry in the platoon and the development of the boundary layer along the platoon. Due to the platoon formation, the boundary layer around trailing lorries becomes thicker, resulting in lower vortex shedding frequencies but larger variances. Moreover, the flow within the platoon seems to be more turbulent as the boundary layer develops, as can be seen from Table 2 and Figure 27. Lorry 5 to 8 clearly suffer from more complex vortex shedding, as a number of

distinct components with relatively high energy can be identified. This is also suggested by the increased variance for the latter four lorries in the platoon.

From a practical view, the variances of the side force coefficients are converted to the std of the equivalent oscillating side forces in full-scale, considering a typical lorry speed of 60 mph. At the same time, the equivalent full-scale frequencies are also derived, as listed in Table 2. Table 2 suggests that the std of the side forces is 107.16 N for a single lorry running at 60 mph. However, the std drops to 96.8 N when trailing lorries are present. As implied in the above discussion on variances, the lorries situated further into the platoon generally suffer from higher std, apart from the last lorry. The highest std is found to be on lorry 7, which yields 211.43 N. The equivalent full-scale frequencies indicate that for the latter four lorries with high std, the oscillating frequencies are approximately 1 Hz.

6. Conclusions

An in-depth numerical investigation of the effects of platooning, including drag performance, flow-vehicle interactions and lateral stability, has been carried out in this work using the DDES technique, considering an eight-lorry platoon with 0.5L inter-vehicle spacing. The numerical simulations were compared with moving model experiments and good agreement has been found. Based on the numerical results, a number of important findings are summarised as follows:

- The results indicate a roughly 15% drop in drag for the first lorry compared to that of an isolated lorry. Significant drag reduction is found for all trailing lorries, which suggests more than 60% reduction can be achieved for the intermediate vehicles. The trend of drag reduction is found to agree with the literature of comparable platoon cases and it is shown that this trend can extend to longer platoons.
- The platoon studied is found to cause very low-velocity regions at the gaps between lorries, leading to low frontal positive pressure and less negative base pressure. The turbulent kinetic energy and Reynolds stresses are concentrated between the gaps of the lorries and the top of the cab.
- Highly turbulent flow was identified on the top and sides of the trailing lorries while the first lorry experiences less turbulent flow conditions.
- The dominant component of TKE and Reynolds stresses is found to be in the streamwise direction and concentrates around the connection region between lorry cab and box for lorry 2 to lorry 8. Moreover, the generation of high TKE is found to exist when the body consists of sharp corners and edges.
- The time-averaged flow field reveals a minor recirculation ring above the cab of lorry 1 and much larger recirculation zones at the rear gaps between the lorries. These recirculation zones are very close to the rear surfaces of the lorries. All trailing lorries have similar size and velocity magnitude, while differences were found on the lead lorry. In contrast, drastic fluctuations are usually found away from the lorry surfaces, and typically, contrary to where the recirculation zones of the averaged flow field occur.
- The power spectral analysis indicates that all lorries in the platoon suffer from oscillating side forces due to vortex shedding at various *St*. The vortex shedding experienced by a lorry in a platoon exhibit more power than that on an isolated lorry, implying that the platoon is more vulnerable to lateral instability than a single lorry.

Due to the platoon formation, the boundary layer around trailing lorries becomes thicker, resulting in lower vortex shedding frequencies but larger variances.

- The variances and *St* are converted to std and frequencies of the equivalent oscillating side forces in full-scale at a typical lorry speed respectively. The std shows lorry 7 suffers from strongest oscillating side forces of 211 N. The oscillating frequencies of the side forces on the latter four lorries with higher std are roughly 1 Hz.

Acknowledgements

This work is carried out on an EPSRC funded project entitled 'The aerodynamics of close running ground vehicles - EP/N004213/1'. The authors thank EPSRC for providing access to computational resources on ARCHER through the UK Applied Aerodynamics Consortium Leadership Project e529. We also acknowledge the use of Athena at HPC Midlands+, which was funded by the EPSRC on grant EP/P020232/1, in this research. The authors would like to also thank BlueBEAR at the University of Birmingham for the computational resources.

Reference

'Platooning'. 2019. Wikipedia. Available: https://es.wikipedia.org/wiki/Platooning [Accessed 20th May 2019].

Altinisik, A., Yemenici, O. & Umur, H. 2015. Aerodynamic Analysis of a Passenger Car at Yaw Angle and Two-Vehicle Platoon. *Journal of Fluids Engineering,* 137**,** 121107-121107-10.

Ashton, N. & Revell, A. 2015. Key factors in the use of DDES for the flow around a simplified car. *International Journal of Heat and Fluid Flow,* 54**,** 236-249.

Baker, C., Dalley, S., Johnson, T., Quinn, A. & Wright, N. 2001. The slipstream and wake of a high-speed train. *Proceedings of the Institution of Mechanical Engineers, Part F: Journal of Rail and Rapid Transit,* 215**,** 83-99.

Blazek, J. 2015. Chapter 7 - Turbulence Modeling. *In:* BLAZEK, J. (ed.) *Computational Fluid Dynamics: Principles and Applications (Third Edition)*. Oxford: Butterworth-Heinemann.

Blocken, B., Toparlar, Y. & Andrianne, T. 2016. Aerodynamic benefit for a cyclist by a following motorcycle. *Journal of Wind Engineering and Industrial Aerodynamics,* 155**,** 1-10.

Blocken, B., Toparlar, Y., Van Druenen, T. & Andrianne, T. 2018. Aerodynamic drag in cycling team time trials. *Journal of Wind Engineering and Industrial Aerodynamics,* 182**,** 128-145.

Bruneau, C.-H., Khadra, K. & Mortazavi, I. 2017. Flow analysis of square-back simplified vehicles in platoon. *International Journal of Heat and Fluid Flow,* 66**,** 43-59.

Cheli, F., Corradi, R., Sabbioni, E. & Tomasini, G. 2011. Wind tunnel tests on heavy road vehicles: Cross wind induced loads—Part 1. *Journal of Wind Engineering and Industrial Aerodynamics,* 99**,** 1000-1010.

Dorigatti, F. 2013. *Rail vehicles in crosswinds: analysis of steady and unsteady aerodynamic effects through static and moving model tests.* University of Birmingham.

Dorigatti, F., Sterling, M., Baker, C. J. & Quinn, A. D. 2015. Crosswind effects on the stability of a model passenger train—A comparison of static and moving experiments. *Journal of Wind Engineering and Industrial Aerodynamics,* 138**,** 36-51.

Ewald, H. 1984. *Aerodynamische Effekte beim Kolonnenfahren (Modelluntersuchungen),* Essen: Haus der Technik.

Flynn, D., Hemida, H. & Baker, C. 2016. On the effect of crosswinds on the slipstream of a freight train and associated effects. *Journal of Wind Engineering and Industrial Aerodynamics,* 156**,** 14-28.

Flynn, D., Hemida, H., Soper, D. & Baker, C. 2014. Detached-eddy simulation of the slipstream of an operational freight train. *Journal of Wind Engineering and Industrial Aerodynamics,* 132**,** 1-12.

Golovanevskiy, V. A., Chmovzh, V. V. & Girka, Y. V. 2012. On the optimal model configuration for aerodynamic modeling of open cargo railway train. *Journal of Wind Engineering and Industrial Aerodynamics,* 107-108**,** 131-139.

Grandemange, M., Gohlke, M. & Cadot, O. 2013. Turbulent wake past a three-dimensional blunt body. Part 1. Global modes and bi-stability. *Journal of Fluid Mechanics,* 722**,** 51-84.

He, M., Hemida, H., Soper, D., Sterling, M. & Baker, C. J. Numerical simulations of flow around lorries in platoon. the Third International Conference in numerical and experimental aerodynamics of road vehicles and trains, 2018a Milan.

He, M., Huo, S., Hemida, H., Soper, D., Sterling, M. & Baker, C. J. Numerical simulations of flow around ground vehicles running in platoon. UK Wind Engineering Society Conference, 2018b Leeds, UK.

Hemida, H. & Krajnović, S. 2009. Transient Simulation of the Aerodynamic Response of a Double-Deck Bus in Gusty Winds. *Journal of Fluids Engineering,* 131**,** 031101-031101-10.

Humphreys, H. & Bevly, D. 2016. Computational Fluid Dynamic Analysis of a Generic 2 Truck Platoon. SAE International.

Kapadia, S., Roy, S., Vallero, M., Wurtzler, K. & Forsythe, J. Detached-Eddy Simulation over a Reference Ahmed Car Model. 2004 Dordrecht. Springer Netherlands, 481-488.

Krajnović, S., Georgii, J. & Hemida, H. DES of the Flow Around a High-Speed Train Under the Influence of Wind Gusts. 7th International ERCOFTAC Symposium on Engineering Turbulence Modeling and Measurements, Limassol, Cyprus: IEEE, 2007.

Lahaye, A., Leroy, A. & Kourta, A. 2014. Aerodynamic characterisation of a square back bluff body flow. *International Journal of Aerodynamics,* 4**,** 43-60.

Li, T., Hemida, H., Zhang, J., Rashidi, M. & Flynn, D. 2018. Comparisons of Shear Stress Transport and Detached Eddy Simulations of the Flow Around Trains. *Journal of Fluids Engineering,* 140**,** 111108-111108-12.

Liaifar, A. 2013. *LIDAR, lasers, and logic: Anatomy of an autonomous vehicle* [Online]. Anatomy of an autonomous vehicle. Available: https://www.digitaltrends.com/cars/lidar-lasers-and-beefed-up-computers-the-intricate-anatomy-of-an-autonomous-vehicle/ [Accessed 27 Feb 2018].

Maddox, S., Squires, K. D., Wurtzler, K. E. & Forsythe, J. R. Detached-Eddy Simulation of the Ground Transportation System. 2004 Berlin, Heidelberg. Springer Berlin Heidelberg, 89-104.

Mcarthur, D., Burton, D., Thompson, M. & Sheridan, J. 2018. An experimental characterisation of the wake of a detailed heavy vehicle in cross-wind. *Journal of Wind Engineering and Industrial Aerodynamics,* 175**,** 364-375.

Michaelian, M. & Browand, F. 2001. Quantifying Platoon Fuel Savings: 1999 Field Experiments. *SAE Transactions,* 110**,** 1401-1410.

Mirzaei, M. & Krajnović, S. Large Eddy Simulations of Flow Around Two Generic Vehicles in a Platoon. 2016 Cham. Springer International Publishing, 283-288.

Morden, J. A., Hemida, H. & Baker, C. J. 2015. Comparison of RANS and Detached Eddy Simulation Results to Wind-Tunnel Data for the Surface Pressures Upon a Class 43 High-Speed Train. *Journal of Fluids Engineering,* 137**,** 041108-041108-9.

Numeca International 2017. HEXPRESS/Hybrid 6.2 User Guide. *In:* NUMECA INTERNATIONAL (ed.).

Openfoam Ltd. 2016. Divergence schemes. *In:* GREENSHIELDS, C. (ed.) *OpenFOAM v4 User Guide.*

Pagliarella, R. M., Watkins, S. & Tempia, A. 2007. Aerodynamic Performance of Vehicles in Platoons: The Influence of Backlight Angles. *SAE Technical Paper Series.* SAE International.

Patel, N., Hemida, H. & Quinn, A. Large-Eddy Simulations of the airflow around a vehicle. 6th European and African Conference on Wind Engineering, EACWE 2013, 2013.

Quinn, A., Sterling, M., Robertson, A. & Baker, C. 2007. An investigation of the wind-induced rolling moment on a commercial vehicle in the atmospheric boundary layer. *Proceedings of the Institution of Mechanical Engineers, Part D: Journal of Automobile Engineering,* 221**,** 1367-1379.

Robertson, F. H., Soper, D., Baker, C. J., Sterling, M. & Hemida, H. An experimental investigation into the aerodynamics of close running road vehicles. 13th UK Conference on Wind Engineering, 2018 Leeds.
Schuetz, T. 2016. Aerodynamics of road vehicles. Fifth Edition / by Thomas Schuetz. ed.: Warrendale, Pennsylvania : SAE International, 2016.
Soper, D. 2016. *The aerodynamics of a container freight train*, Springer.
Soper, D., Baker, C. & Sterling, M. 2014. Experimental investigation of the slipstream development around a container freight train using a moving model facility. *Journal of Wind Engineering and Industrial Aerodynamics,* 135**,** 105-117.
Soper, D., Gallagher, M., Baker, C. & Quinn, A. 2017. A model-scale study to assess the influence of ground geometries on aerodynamic flow development around a train. *Proceedings of the Institution of Mechanical Engineers, Part F: Journal of Rail and Rapid Transit,* 231**,** 916-933.
Spalart, P. & Allmaras, S. A one-equation turbulence model for aerodynamic flows. 30th aerospace sciences meeting and exhibit, 1992. 439.
Spalart, P. R., Deck, S., Shur, M. L., Squires, K. D., Strelets, M. K. & Travin, A. 2006. A New Version of Detached-eddy Simulation, Resistant to Ambiguous Grid Densities. *Theoretical and Computational Fluid Dynamics,* 20**,** 181.
Sterling, M., Baker, C. J., Jordan, S. C. & Johnson, T. 2008. A study of the slipstreams of high-speed passenger trains and freight trains. *Proceedings of the Institution of Mechanical Engineers, Part F: Journal of Rail and Rapid Transit,* 222**,** 177-193.
Sterling, M., Quinn, A. D., Hargreaves, D. M., Cheli, F., Sabbioni, E., Tomasini, G., Delaunay, D., Baker, C. J. & Morvan, H. 2010. A comparison of different methods to evaluate the wind induced forces on a high sided lorry. *Journal of Wind Engineering and Industrial Aerodynamics,* 98**,** 10-20.
T.F.I. 2011. Turbulent Flow Instrumentation - Cobra Probe - Getting started guide

Taylor, J. 1997. An Introduction to Error Analysis: The Study of Uncertainties in. *Published by University Science Books, 648 Broadway, Suite 902, New York, NY 10012, 1997.*
Travin, A., Shur, M., Strelets, M. & Spalart, P. 2000. Detached-Eddy Simulations Past a Circular Cylinder. *Flow, Turbulence and Combustion,* 63**,** 293-313.
Tsuei, L. & Savaş, Ö. 2001. Transient aerodynamics of vehicle platoons during in-line oscillations. *Journal of Wind Engineering and Industrial Aerodynamics,* 89**,** 1085-1111.
Uystepruyst, D. & Krajnović, S. 2013. LES of the flow around several cuboids in a row. *International Journal of Heat and Fluid Flow,* 44**,** 414-424.
Vegendla, P., Sofu, T., Saha, R., Madurai Kumar, M. & Hwang, L.-K. 2015. Investigation of Aerodynamic Influence on Truck Platooning. SAE International.
Volpe, R., Devinant, P. & Kourta, A. 2015. Experimental characterization of the unsteady natural wake of the full-scale square back Ahmed body: flow bi-stability and spectral analysis. *Experiments in Fluids,* 56**,** 99.
Wang, S., Bell, J. R., Burton, D., Herbst, A. H., Sheridan, J. & Thompson, M. C. 2017. The performance of different turbulence models (URANS, SAS and DES) for predicting high-speed train slipstream. *Journal of Wind Engineering and Industrial Aerodynamics,* 165**,** 46-57.
Wasserman, S. 2016. *Choosing the Right Turbulence Model for Your CFD Simulation* [Online]. Engineering.com. Available: https://www.engineering.com/DesignSoftware/DesignSoftwareArticles/ArticleID/13743/Choosing-the-Right-Turbulence-Model-for-Your-CFD-Simulation.aspx [Accessed 08 February 2018].

Watkins, S. & Vino, G. 2008. The effect of vehicle spacing on the aerodynamics of a representative car shape. *Journal of wind engineering and industrial aerodynamics,* 96**,** 1232-1239.

Watts, A. 2015. *Computational Characterization of Drag Reduction for Platooning Heavy Vehicles.* Master Master Thesis, Auburn University.

Zabat, M., Stabile, N., Farascaroli, S. & Browand, F. 1995. The aerodynamic performance of platoons: A final report.